

Nuclear Hartree-Fock Calculations on Parallel Computers

Thesis by
Bing-Qing Chen

In Partial Fulfillment of the Requirements
for the Degree of
Doctor of Philosophy



California Institute of Technology
Pasadena, California

1994
(Submitted January 5, 1994)

©1994

Bing-Qing Chen

All rights reserved

Acknowledgements

I would like to thank my thesis advisor Steve Koonin for stimulating discussions and his encouragement. Among many people who have contributed to this work with their fruitful discussions, I would like to especially thank Paul-Henri Heenen, Peter Vogel, Mort Weiss and Paul Bonche. I would also like to acknowledge the hospitality of the Nuclear Theory group of the Lawrence Livermore National Laboratory where this work was initiated. This research was performed in part using the Intel Touchstone Delta System operated by Caltech on behalf of the Concurrent Supercomputing Consortium.

Abstract

Hartree-Fock (HF) calculations have had remarkable success in describing large nuclei at high spin, temperature and deformation. To allow full range of possible deformations, the Skyrme HF equations can be discretized on a three-dimensional mesh. However, such calculations are currently limited by the computational resources provided by traditional supercomputers. To take advantage of recent developments in massively parallel computing technology, we have implemented the LLNL Skyrme-force static and rotational HF codes on Intel's DELTA and GAMMA systems at Caltech.

We decomposed the HF code by assigning a portion of the mesh to each node, with nearest neighbor meshes assigned to nodes connected by communication channels. This kind of decomposition is well-suited for the DELTA and the GAMMA architecture because the only non-local operations are wave function orthogonalization and the boundary conditions of the Poisson equation for the Coulomb field.

Our first application of the HF code on parallel computers has been the study of identical superdeformed (SD) rotational bands in the Hg region. In the last ten years, many SD rotational bands have been found experimentally. One very surprising feature found in these SD rotational bands is that many pairs of bands in nuclei that differ by one or two mass units have nearly identical deexcitation gamma-ray energies. Our calculations of the five rotational bands in ^{192}Hg and ^{194}Pb show that the filling of specific orbitals can lead to bands with deexcitation gamma-ray energies differing by at most 2 keV in nuclei differing by two mass units and over a range of angular momenta

comparable to that observed experimentally. Our calculations of SD rotational bands in the Dy region also show that twinning can be achieved by filling or emptying some specific orbitals.

The interpretation of future precise experiments on atomic parity nonconservation (PNC) in terms of parameters of the Standard Model could be hampered by uncertainties in the atomic and nuclear structure. As a further application of the massively parallel HF calculations, we calculated the proton and neutron densities of the Cesium isotopes from $A = 125$ to $A = 139$. Based on our good agreement with experimental charge radii, binding energies, and ground state spins, we conclude that the uncertainties in the ratios of weak charges are less than 10^{-3} , comfortably smaller than the anticipated experimental error.

Table of Contents

| | | |
|----------|---|-----------|
| 1 | Nuclear Hartree-Fock Method | 4 |
| 1.1 | Introduction | 4 |
| 1.2 | Effective interactions | 5 |
| 1.3 | Constrained Hartree-Fock equations | 7 |
| 1.3.1 | Hartree-Fock energy | 7 |
| 1.3.2 | Hartree-Fock equations | 10 |
| 1.3.3 | Pairing energy | 11 |
| 1.3.4 | Constraint | 12 |
| 1.4 | Numerical procedures | 14 |
| 2 | Implementation on Parallel Computers | 17 |
| 2.1 | Introduction | 17 |
| 2.2 | Decomposition method | 19 |
| 2.3 | Optimizing the communication speed | 21 |
| 2.4 | Performance and efficiency | 22 |
| 2.5 | Conclusion | 24 |
| 3 | Cranked Hartree-Fock Study of Superdeformed Rotational Bands | 27 |
| 3.1 | Introduction | 27 |
| 3.2 | Identical bands | 28 |

| | | |
|----------|---|-----------|
| 3.3 | Cranked Hartree-Fock method | 31 |
| 3.4 | Identical SD Bands in $A = 190$ mass region | 34 |
| 3.5 | Identical SD Bands in $A = 150$ mass region | 46 |
| 3.6 | Conclusion | 52 |
| 4 | Atomic parity nonconservation and neutron radii in cesium isotopes | 54 |
| 4.1 | Introduction | 54 |
| 4.2 | Nuclear Hartree-Fock calculations | 58 |
| 4.3 | Comparison with experiment | 59 |
| 4.4 | Estimated uncertainties in PNC effects | 69 |
| 4.5 | Conclusion | 74 |

List of Tables

| | | |
|-----|--|----|
| 1.1 | Symmetry properties of $\psi_{i,\alpha}$ | 10 |
| 2.1 | Computational time for 200 iterations of ^{208}Pb | 25 |
| 2.2 | Computational time for 200 iterations of ^{40}Ca | 25 |
| 3.1 | Properties of the five bands constructed | 37 |
| 3.2 | Properties of the single particle orbitals considered | 44 |
| 4.1 | Neutron and proton radii from SkM* | 61 |
| 4.2 | Neutron and proton radii from SIII | 61 |
| 4.3 | Radiatively corrected weak charges $Q_W(N, Z)$ and nuclear structure correction Q_W^{nuc} | 72 |

List of Illustrations

| | | |
|-----|---|----|
| 3.1 | Deformation energy curve for ^{192}Hg and ^{194}Pb | 35 |
| 3.2 | Neutron and proton Routhians for ^{192}Hg | 36 |
| 3.3 | Rotational energies for the various bands constructed here | 39 |
| 3.4 | ΔE_γ between the $A = 194$ bands and the ^{192}Hg band | 40 |
| 3.5 | Dynamical moments of inertia \mathcal{J}_2 for the five bands constructed. | 41 |
| 3.6 | Quadrupole moment as a function of J_z | 43 |
| 3.7 | Neutron and proton Routhians for ^{152}Dy | 47 |
| 3.8 | Dynamical moments of inertia \mathcal{J}_2 for the ^{151}Tb and ^{152}Dy bands. | 50 |
| 3.9 | ΔE_γ between the ^{151}Dy bands and the ^{152}Dy band | 51 |
| 4.1 | Deformation energy curve for Cs isotopes | 60 |
| 4.2 | Calculated and experimental isotope shifts $\delta\langle r_p^2 \rangle$ in cesium using SkM* | 63 |
| 4.3 | Calculated and experimental isotope shifts $\delta\langle r_p^2 \rangle$ in cesium using SIII | 64 |
| 4.4 | Calculated change in neutron radii $\delta\langle r_n^2 \rangle$ in cesium using SkM* and SIII | 67 |

Introduction

Computational resources present a significant limitation in many fields of theoretical physics nowadays. Although the speed of conventional sequential CPUs has been increasing steadily in the past ten years, they are still far from fulfilling the computational need of current theoretical physics. However, with the recent advent of massively parallel computing technology, it is now possible to connect a large number of independent CPU chips, called *nodes*, by high speed communication channels and have them perform tasks not previously possible on conventional computers. Although the speed of a single CPU chip might soon reach its limit, the potential of parallel computing is virtually unlimited as it is always possible to put more CPUs together. Therefore, parallel computing represents the future of high performance computing.

One of the most exciting developments in the recent parallel computing history has been the availability of the Intel Touchstone DELTA and GAMMA systems to a consortium lead by Caltech. Both the DELTA and GAMMA systems are built from the Intel i860 microchips which can perform a peak of 60 million double precision floating point operations per second (MFLOPS). The DELTA system consists of 512 nodes connected by a 32×16 rectangular mesh. The GAMMA system, being a prototype of the DELTA system, consists of 64 nodes connected by 8-dimensional hypercube architecture. With 512 nodes, DELTA has a peak speed of 30 GFLOPS, much faster than any sequential systems available today. However, the current compiler technology is still not able to produce code for i860 to operate at optimal condition and the usual speed compiler can

produce only about 5-10 MFLOPS per node. Each node in both machines has 2 million double precision words (MW) of memory. Because each node can only directly access its own private memory, inter-node communications are necessary for one node to access the memory of the other nodes. Besides the difference in number of nodes and connection topology between these two machines, the inter-node communication speed on DELTA is several times faster than it is on GAMMA.

In order to see how well the parallel computing technology can be adapted to the future computational need, it is interesting to see how well the current parallel computers perform in some particular fields. There are certain programs which can be trivially parallelized in that one can just have each node in a parallel computer run the program with different input parameters and combine the answers of each node at the end. These kind of programs have nearly no inter-node communications and thus have nearly 100% of efficiency and can really take advantage of the parallel computer. However, most realistic programs cannot fit into the memory of one single node or take far too long to complete in one node. To take advantage of parallel computing, these kind of programs have to be decomposed into small parts and have each node work on a different part. In order to complete part of the calculations in one node, the data in other nodes are usually needed. Therefore, inter-node communications are inevitable for these kinds of decomposition. Although the current state of the art CPUs can perform in excess of 60 MFLOPS, the inter-node communication speed is generally smaller than 1 MW per second. In the case of DELTA, the average communication speed is only about 0.3 MW per second. Therefore, the communication speed is still the bottleneck of most parallel implementations today. Because of this, a program can only be implemented efficiently on a parallel computer if the amount of inter-node communications is orders of magnitude smaller than the amount of numerical calculations. Fortunately, there are a large number of programs that can meet this criteria. It is the purpose of this research to explore how well a certain class of scientific applications can be adapted to the current

parallel computers.

Fully self-consistent nuclear Hartree-Fock (HF) calculations have had remarkable success in describing heavy nuclei at high spin, temperature and deformation. Because the rich variety of shapes nuclei can have, it is very important to be able to describe all kinds of deformations in a nuclear model. To allow full range of possible deformations, the nuclear wave functions need to be described on a three-dimensional mesh instead of relying on an expansion in a limited basis. However, such calculations are very computationally intensive and are severely limited by the computational resources provided by traditional supercomputers. Fortunately, these type of calculations are well suited to parallel computing architecture because the Hamiltonian matrix that is involved in such calculations is very sparse and banded. In this research, we will discuss the ability of performing such calculations on massively parallel computers and will apply the method to study some real physical problems.

This thesis is organized as follows. In Chapter 1, we discuss the nuclear HF method and the numerical algorithms for solving it. In Chapter 2, we show how we are able to implement these algorithms on the DELTA and GAMMA systems and what is the performance we get out of them. In Chapter 3, we present the results of the study of the recently discovered identical rotational bands with this method. In Chapter 4, we apply the method to the calculation of the proton and neutron radii in a chain of cesium isotopes which are crucial to the interpretation of the future precise experiments on atomic parity violation in terms of parameters of the Standard Model.

Chapter 1

Nuclear Hartree-Fock Method

1.1 Introduction

The basic assumption of low-energy nuclear theory is that a nucleus can be described as a set of non-relativistic nucleons interacting via a two-body interaction. Over the last half century, this assumption has been verified with great successes. However, the nuclear many-body problem is far from being solved. Because of the complexity of the basic two body nucleon-nucleon interactions and the large number degrees of freedom involved, exact solutions for medium to heavy nuclei are still impossible. As a first approximation, so called mean field approximation, the assembly of strongly interacting nucleons can be approximated by a set of independent nucleons moving in a self-generated mean potential field. This approximation, while rather crude at first sight, has successfully described the principal properties of nuclei throughout the periodic table. This suggests that the Pauli principle plays an important role in simultaneously building up a mean-field and suppressing the strong N-N interaction terms.

In section 1.2, we will discuss the basic ingredients for the Hartree-Fock calculations, namely the nucleon-nucleon force. In section 1.3, we describe the Hartree-Fock method in detail and in section 1.4 we show the numerical procedure for solving the problem.

1.2 Effective interactions

It is well known that the bare nucleon-nucleon force includes a strong repulsive core at short distances, a strong attraction at intermediate distances, and a long-range force dominated by one-pion exchange. However, because of the strong repulsion at short distances, these bare nucleon-nucleon forces are very ill behaved from a numerical point of view and cannot be treated straightforwardly by the usual many-body techniques. A way out of this situation is to use, in place of the bare interaction, a so-called effective interaction, which is itself an infinite sum of scattering processes of two nucleons in a nuclear medium. The effective interaction is rather well behaved and can be derived from the bare nucleon-nucleon force. Unfortunately, the rather complex analytical structure of these effective interactions derived from bare nucleon-nucleon forces has prevented their systematic use in describing nuclear properties.

In most of the so-called microscopic descriptions of the nucleus, one uses *phenomenological effective forces*, which are constructed on the basis of these considerations, but depend on some parameters that are adjusted to fit experimental data. Although less fundamental, this approach is extremely useful: it allows one to do calculation in regions where realistic calculations become impractical. It also allows one to make systematic studies with minimal numerical work.

There exist, of course, an enormous number of different phenomenological interactions that have been applied to problems in nuclear physics. Two most notable examples, namely the Skyrme[1] and Gogny forces, are specifically devised for HF and HFB calculations, taking into account all nucleons. Therefore they do not assume a priori separation between a core and some valence nucleons. The Skyrme force, being a zero range force with finite range property approximated by momentum dependence, is particularly well suited for HF calculations and parallel computing implementation (see below). Therefore, this research is focused on the HF calculations using the Skyrme forces.

The generalized Skyrme force (including all possible spin-exchange terms and zero-range density-dependent interaction) can be parametrized as,

$$\begin{aligned}
 V_s = & \quad t_0(1 + x_0 P_\sigma)\delta + \frac{1}{2}t_1(1 + x_1 P_\sigma)(\mathbf{k}'^2\delta + \delta\mathbf{k}^2) + t_2(1 + x_2 P_\sigma)\mathbf{k}' \cdot \delta\mathbf{k} \\
 & + \frac{1}{6}t_3\rho^\alpha\delta + iW(\boldsymbol{\sigma}_1 + \boldsymbol{\sigma}_2) \cdot \mathbf{k}' \times \delta\mathbf{k} ,
 \end{aligned} \tag{1.1}$$

where t_{0-3}, x_{0-2} and W are the adjustable parameters, and

$$\begin{aligned}
 \delta & \equiv \delta(\mathbf{r} - \mathbf{r}') , \\
 \mathbf{k} & = \frac{1}{2i}(\nabla_1 - \nabla_2) , \\
 \mathbf{k}' & = \mathbf{k}^\dagger , \\
 P_\sigma & = \frac{1}{2}(1 + \boldsymbol{\sigma}_1 \cdot \boldsymbol{\sigma}_2) .
 \end{aligned} \tag{1.2}$$

The parameter t_0 describes a pure δ -force with a spin-exchange terms; t_1 and t_2 simulate an effective range with spin exchanges; the density dependent t_3 term has the same expectation value as a zero-range three-body interaction for $\alpha = 1$; the fifth term represents a two-body spin-orbit interaction.

The few adjustable parameters in the Skyrme force are adjusted to fit the various bulk properties (energy per nucleon, compression modulus, symmetry energy, etc.), and properties of several doubly magic nuclei (binding energies, charge radii, etc.)[2]. There are many different sets of parameters resulting from different fits. In this research, we have used two kinds of Skyrme forces (SkM* and SIII). The SIII force [3], which is the most successful force proposed in the 1970's, features a good single-particle spectrum among other qualities. It has, however, a nuclear-matter compression modulus $K_\infty = 355$ MeV which is too large compared to the empirical value of $K_\infty = (220 \pm 10)$ MeV and it over predicts fission barrier heights by nearly a factor of two. The SkM* [6, 7] force has reasonable actinide fission barrier heights and a reasonable compression modulus of

$K_\infty = 215$ MeV. Both forces have been successfully employed to describe the nuclear ground state and rotational properties in several regions of the periodic table.

1.3 Constrained Hartree-Fock equations

1.3.1 Hartree-Fock energy

Assume that the ground state of a nucleus is represented by a Slater determinant Φ of single-particle states Φ_i ,

$$\Phi(x_1, x_2, \dots, x_A) = \frac{1}{\sqrt{A!}} \det |\Phi_i(x_j)|, \quad (1.3)$$

where x denotes the set \mathbf{r}, σ, q of space, spin and isospin coordinates ($q = +\frac{1}{2}$ for proton, $q = -\frac{1}{2}$ for neutron). Due to the zero-range nature of the Skyrme force, the expectation value of the total HF energy E associated with a Skyrme-like force can be written as the integral of a local Hamiltonian density $\mathcal{H}(\mathbf{r})$:

$$E = \int \mathcal{H}(\mathbf{r}) d^3r. \quad (1.4)$$

For time-reversal invariant, uncorrelated wave functions, $\mathcal{H}(\mathbf{r})$ can be expressed in terms of three densities ρ , τ and $\nabla \cdot \mathbf{J}$ [8],

$$\begin{aligned} \mathcal{H}(\mathbf{r}) = & \frac{\hbar^2}{2m} \left(1 - \frac{1}{A}\right) \tau + B_1 \rho^2 + B_2 (\rho_n^2 + \rho_p^2) + B_3 \rho \tau + B_4 (\rho_n \tau_n + \rho_p \tau_p) \\ & + B_5 \rho \Delta \rho + B_6 (\rho_n \Delta \rho_n + \rho_p \Delta \rho_p) + B_7 \rho^{2+\alpha} + B_8 \rho^\alpha (\rho_n^2 + \rho_p^2) \\ & + B_9 (\rho \nabla \cdot \mathbf{J} + \rho_n \nabla \cdot \mathbf{J}_n + \rho_p \nabla \cdot \mathbf{J}_p) + E_C. \end{aligned} \quad (1.5)$$

The coefficients $B_i (i = 1, \dots, 9)$ in equation (1.5) can be expressed in terms of the parameters t_i , x_i , α and W of the Skyrme force,

$$\begin{aligned}
B_1 &= \frac{1}{2}t_0(1 + \frac{1}{2}x_0), & B_2 &= -\frac{1}{2}(x_0 + \frac{1}{2}), \\
B_3 &= \frac{1}{4}(t_1(1 + \frac{1}{2}x_1) + t_2(1 + \frac{1}{2}x_2)), & B_4 &= -\frac{1}{4}(t_1(x_1 + \frac{1}{2}) - t_2(x_2 + \frac{1}{2})), \\
B_5 &= -\frac{1}{16}(3t_1(1 + \frac{1}{2}x_1) - t_2(1 + \frac{1}{2}x_2)), & B_6 &= -\frac{1}{16}(3t_1(x_1 + \frac{1}{2}) + t_2(x_2 + \frac{1}{2})), \\
B_7 &= \frac{1}{12}t_3(1 + \frac{1}{2}x_3), & B_8 &= -\frac{1}{12}t_3(x_3 + \frac{1}{2}), \\
B_9 &= -\frac{1}{2}W.
\end{aligned} \tag{1.6}$$

The Coulomb energy E_C in expression (1.5) is calculated from proton density ρ_p as

$$E_C = \frac{1}{2}e^2 \int d^3r_1 d^3r_2 \frac{\rho_p(\mathbf{r}_1)\rho_p(\mathbf{r}_2)}{|\mathbf{r}_1 - \mathbf{r}_2|} - \frac{3e^2}{4} \left(\frac{3}{\pi}\right)^{1/3} \int d^3r \rho_p^{4/3}(\mathbf{r}), \tag{1.7}$$

where the exchange energy is approximated by the Slater approximation [2]. As in Ref. [4] the center-of-mass recoil energy has been approximated as $-\sum \mathbf{p}_i^2/2Am$.

The densities ρ, τ and $\nabla \cdot \mathbf{J}$ can be expressed in terms of single-particle wave functions Φ_i as

$$\begin{aligned}
\rho(\mathbf{r}) &= \sum_{i,\sigma} v_i^2 |\Phi_i(\mathbf{r}, \sigma)|^2, & \tau(\mathbf{r}) &= \sum_{i,\sigma} v_i^2 |\nabla \Phi_i(\mathbf{r}, \sigma)|^2, \\
\nabla \cdot \mathbf{J}(\mathbf{r}) &= -i \sum_{i,\sigma,\sigma'} v_i^2 \nabla \Phi_i^*(\mathbf{r}, \sigma) \times \nabla \Phi_i(\mathbf{r}, \sigma') \cdot \langle \sigma | \boldsymbol{\sigma} | \sigma' \rangle,
\end{aligned} \tag{1.8}$$

where $\Phi_i(\mathbf{r}, \sigma)$ denotes the component of the i th individual wave function with spin $\frac{1}{2}\sigma (\sigma = \pm 1)$ along the z -direction, and v_i^2 denotes its BCS occupation factor (see below).

Several symmetry properties can be used to simplify the calculations

1. parity

$$\hat{P}\Phi_i(\mathbf{r}, \sigma) = \Phi_i(-\mathbf{r}, \sigma) = p_i \Phi_i(\mathbf{r}, \sigma), \quad p_i = \pm 1; \tag{1.9}$$

2. z -signature

$$\exp\{i\pi(\hat{J}_z - \frac{1}{2})\}\Phi_i(x, y, z, \sigma) = \sigma\Phi_i(-x, -y, z, \sigma) = \eta_i\Phi_i(x, y, z, \sigma), \quad \eta_i = \pm 1, \quad (1.10)$$

Since the Hamiltonian (1.5) is time-reversal invariant, the single-particle orbitals can be grouped in time-reversed pairs Φ_i and $\Phi_{\bar{i}}$ such that,

$$\Phi_{\bar{i}}(\mathbf{r}, \sigma) = \hat{T}\Phi_i(\mathbf{r}, \sigma) = \sigma\Phi_i^*(\mathbf{r}, -\sigma). \quad (1.11)$$

It is therefore sufficient to solve the HF equations for one member of the pair in 1/8th of the total configuration space. We choose to do this for the positive z -signature orbitals.

However, the parity symmetry will have to be relaxed if one wishes to study the octupole degrees of freedom in a nucleus. The time-reversal symmetry is also broken if one adds a cranking term to the Hamiltonian to study the nuclear rotational properties. These problems will be discussed in the following chapters.

Because the spin-orbit interaction in Eq. (1.5) is complex, each wave function has to be described by four real wave functions $\psi_{i,\alpha}(\mathbf{r})$, ($\alpha = 1, \dots, 4$)

$$\Phi_i = \begin{pmatrix} \psi_{i,1}(\mathbf{r}) \\ \psi_{i,2}(\mathbf{r}) \\ \psi_{i,3}(\mathbf{r}) \\ \psi_{i,4}(\mathbf{r}) \end{pmatrix} = \begin{pmatrix} \text{Re } \Phi_i(\mathbf{r}, +) \\ \text{Im } \Phi_i(\mathbf{r}, +) \\ \text{Re } \Phi_i(\mathbf{r}, -) \\ \text{Im } \Phi_i(\mathbf{r}, -) \end{pmatrix}. \quad (1.12)$$

The parity p_i and z -signature $\eta_i = +1$, of the orbital Φ_i induce symmetry properties of the component $\Psi_{i,\alpha}$ with respect to $x = 0$, $y = 0$, and $z = 0$ planes. These are summarized in table 1.1.

Table 1.1: Symmetry properties of $\psi_{i,\alpha}$ with respect to $x = 0, y = 0, z = 0$ planes

| | x | y | z |
|--------------|-----|-----|--------|
| $\psi_{i,1}$ | + | + | p_i |
| $\psi_{i,2}$ | - | - | p_i |
| $\psi_{i,3}$ | - | + | $-p_i$ |
| $\psi_{i,4}$ | + | - | $-p_i$ |

1.3.2 Hartree-Fock equations

The Hartree-Fock equations for Skyrme force are obtained by making the total Hartree-Fock energy stationary with respect to individual variation of single-particle states Φ_i , with the condition that Φ_i are normalized

$$\delta \left(E - \sum_i v_i^2 e_i \int |\Phi_i(\mathbf{r}, \sigma)|^2 d^3r \right) = 0, \quad (1.13)$$

where $v_i^2 e_i$ is a Lagrange multiplier. A variation of Eq. (1.13) against $\Phi_i^*(\mathbf{r}, \sigma)$ gives,

$$\begin{aligned} h\Phi_i(\mathbf{r}, \sigma) &= e_i \Phi_i(\mathbf{r}, \sigma), \\ h\Phi_i(\mathbf{r}, \sigma) &= \sum_{\sigma'} \left\{ -\nabla \frac{\hbar^2}{2m_q^*(\mathbf{r})} \nabla \delta_{\sigma\sigma'} + U_q(\mathbf{r}) \delta_{\sigma\sigma'} \right. \\ &\quad \left. + i\mathbf{W}_q(\mathbf{r}) \cdot (\langle \sigma | \boldsymbol{\sigma} | \sigma' \rangle \times \nabla) \right\} \Phi_i(\mathbf{r}, \sigma'), \end{aligned} \quad (1.14)$$

where the effective mass m_q^* and potential field U_q and W_q are given by

$$\begin{aligned} \frac{\hbar^2}{2m_q^*} &= \frac{\hbar^2}{2m_q} + B_3\rho + B_4\rho_q, \\ U_q(\mathbf{r}) &= 2B_1\rho + 2B_2\rho_q + B_3\tau + B_4\tau_q + 2B_5\Delta\rho + 2B_6\Delta\rho_q + (2 + \alpha)B_7\rho^{1+\alpha} \\ &\quad B_8(\alpha\rho^{\alpha-1} \sum_q \rho_q^2 + 2\rho^\alpha \rho_q) + B_9(\nabla \cdot \mathbf{J} + \nabla \cdot \mathbf{J}_q) + \delta_{g,+\frac{1}{2}} V_C(\mathbf{r}), \\ \mathbf{W}_q(\mathbf{r}) &= -B_9(\nabla\rho + \nabla\rho_q), \end{aligned} \quad (1.15)$$

where the V_C is given by

$$V_C = e^2 \int d^3r' \frac{\rho_p(\mathbf{r}')}{|\mathbf{r} - \mathbf{r}'|} - e^2 \left(\frac{3}{\pi}\right)^{\frac{1}{3}} \rho_p(\mathbf{r})^{\frac{1}{3}} . \quad (1.16)$$

1.3.3 Pairing energy

Pairing correlations have to be taken into account for realistic description of medium and heavy nonmagic shell nuclei. This work does not make use of the modified Skyrme interactions which have been shown to provide reasonable values of pairing matrix elements in the vicinity of the Fermi energy [5]. Instead, we adopt a more empirical point of view and choose to describe pairing between identical nucleons with a BCS formalism using a simple constant strength seniority force. We also assume that the paired states are the two time-reversed orbitals Φ_i and $\Phi_{\bar{i}}$.

Denoting G the strength of the pairing interaction, the HF energy plus pairing energy for even-even nuclei can be expressed as,

$$E^{\text{HF}} = \sum_{i>0} 2v_i^2 e_i - G \sum_{kl>0} f_k f_l (u_k v_k)(u_l v_l) , \quad (1.17)$$

where e_i are the single particle energies and u_i, v_i are BCS occupation numbers. The f_k 's are cut-off factors which depend on the difference $e_i - \lambda$ between the HF single-particle energy of the orbital and the Fermi energy according to the formula

$$f_i = \left(1 + \exp\left(\frac{e_i - \lambda - \Delta e}{\mu}\right)\right)^{-1} . \quad (1.18)$$

These factors forbid the unrealistic pairing of highly excited states which is known to cause divergence in a state-independent seniority interaction. In the definition of f_i 's the quantity Δe fixes the energy interval within which pairing is effectively acting. As typical gaps are about 1 MeV, we choose Δe to be 5 MeV. The value μ which determines the

smoothness of the cut-off is not critical and is chosen to be 0.5MeV here. Note that the cut-off is non-symmetric as it only cuts off those states above the Fermi level. Because G is fitted to experimental pairing gap, this is not important as long as we do it consistently.

The minimization of Eq. (1.17) is performed with respect to the variations of u_i and v_i under the constraints,

$$\begin{aligned} u_i^2 + v_i^2 &= 1 , \\ 2 \sum_{i>0} v_i^2 &= N_q , \end{aligned} \tag{1.19}$$

where N_q is neutron or proton number. We thus obtain the usual BCS equations with state-dependent gaps Δ_i which can be expressed in terms of a single quantity Δ as

$$\begin{aligned} \Delta_i &= f_i \Delta , \\ \Delta &= \frac{1}{2} G \sum_{i>0} \frac{f_i \Delta}{\sqrt{(e_i - \lambda_q)^2 + f_i \Delta^2}} , \\ v_i^2 &= \frac{1}{2} \left[1 - \frac{e_i - \lambda_q}{\sqrt{(e_i - \lambda_q)^2 + f_i \Delta^2}} \right] . \end{aligned} \tag{1.20}$$

The λ_q 's are Fermi energies chosen so that the second part of Eq. (1.19) are satisfied.

The strength of seniority force G is adjusted so that the gap energies obtained from the BCS equations are consistent with experimental odd-even nuclei binding energy differences. See Ref. [8] for more details about the procedure.

1.3.4 Constraint

Unrestricted HF calculations give only one point on the energy surface, namely the local minimum. It is often interesting to calculate the energy surface as a function of one (or several) collective parameters Q , such as quadrupole, octupole and hexadecapole

deformations. In order to calculate the energy surface as a function of deformation, one must add an external constraint field to the Hamiltonian.

For each deformation we want to constrain, a quadratic constraint term is added to the HF energy Eq. (1.5) as described in Ref. [9]. The total functional to be minimized is thus given by

$$\int \mathcal{H}(\mathbf{r})d^3r + \sum_Q C_Q (\langle Q \rangle - \mu_Q)^2 , \quad (1.21)$$

where C_Q is a constraining strength which is chosen so that the energy from the constraint field is about a few MeV. $\langle Q \rangle$ is the average moment at each iteration and μ_Q is a parameter that is adjusted during iterations to obtain

$$\langle Q \rangle = Q_0 , \quad (1.22)$$

where Q_0 is the desired deformation moment.

Of all the possible deformations in a nucleus, the quadrupole degree's of freedom is the most important one. Quadrupole deformation energy surfaces are obtained with a constraint on the mass quadrupole tensor $Q_{ij} = (3x_i x_j - r^2 \delta_{ij})$. The symmetry properties (1.9, 1.10) of the wave function Φ_i ensure that the principal axes of inertia lie along the coordinate axes. The quadrupole tensor is therefore diagonal and its principal values Q_i can be expressed in terms of two quantities Q_0 and γ as

$$Q_i = Q_0 \cos(\gamma + i\frac{2}{3}\pi), \quad i = 1, 2, 3 , \quad (1.23)$$

where Q_0 and γ satisfy the inequalities

$$Q_0 \geq 0, \quad 0 \leq \gamma \leq \frac{1}{3}\pi . \quad (1.24)$$

Practically, the values of the three constraints Q_i are computed from the desired values

of Q_0 and γ and inserted into Eq. 1.21.

1.4 Numerical procedures

The numerical approximation to the HF energy E is obtained by a discretization of the configuration space on a three-dimensional rectangular mesh. The mesh spacing Δx is the same in all three directions and the abscissae of the mesh points are $(n + \frac{1}{2})\Delta x$. The first-order differentiations in the HF equations are approximated by 7-point finite difference [10].

It was found that to obtain similar accuracy for all terms in the functional \mathcal{H} , it is necessary to use a better algorithm for kinetic energy $(\hbar^2/2m)\tau$. This is done by rewriting the corresponding contribution to the energy E as

$$\int \tau d^3r = - \int d^3r \sum_{i\alpha} \Phi_{i,\alpha} \Delta \Phi_{i,\alpha} , \quad (1.25)$$

and using a 9-point approximation to evaluate the Laplacian [11]. The same scheme is employed to compute the $\rho\Delta\rho$ terms in \mathcal{H} .

The discretized version of the HF equations (1.5) is obtained by a direct variation of the *discretized approximation* to the energy E , with respect to the components $\Psi_{i,\alpha}$ at the mesh points.

The Coulomb energy, Eq. (1.7), is computed by solving the Poisson equation for Coulomb potential

$$\Delta\phi(\mathbf{r}) = -4\pi e\rho_p(\mathbf{r}) \quad (1.26)$$

using conjugate gradient method. The Laplacian in Eq. (1.26) is approximated by 3-point finite differences. The boundary conditions for the Coulomb potential are approximated by a multipole expansion.

Our task is to solve the single particle wave functions Φ_i in the discretized version

of Eq. (1.14) self-consistently. An iterative method, known in nuclear physics as the imaginary time-step method[12] is employed here. At each iteration, we obtain the new wave functions as

$$\begin{aligned}\tilde{\Phi}_i^{(n+1)} &= \left[1 - h(\rho^{(n)}, \tau^{(n)}, \nabla \cdot \mathbf{J}^{(n)})\Delta t\right] \Phi_i^{(n)} \approx e^{-h\Delta t} \Phi_i^{(n)}, \\ \Phi^{(n+1)} &= \mathcal{O}[\tilde{\Phi}_i^{(n+1)}],\end{aligned}\tag{1.27}$$

where (n) denotes iteration number, while \mathcal{O} denotes Gram-Schmidt orthonormalization operator (defined below) which is necessary because the imaginary time step evolution operator does not preserve wave function orthonormalization. The initial single particle wave functions $\Phi_i^{(0)}$ are chosen to be the eigenstates of the Nilsson Hamiltonian [13],

$$\mathcal{H} = -\frac{\hbar^2}{2m}\Delta + \frac{m}{2}\omega_{\perp}^2(x^2 + y^2) + \frac{m}{2}\omega_z^2 z^2 + C\mathbf{1} \cdot \mathbf{s} + D\mathbf{I}^2.\tag{1.28}$$

At each iteration, we have to calculate the h in Eq. (1.27) acting on the wave functions. This requires knowledges of ρ and τ which depend on v_i^2 and thus e_i . Since before the system converges, the h is not diagonalized, we approximate e_i to be the expectation values of single particle wave functions at previous iteration,

$$e_i^n = \int d^3r \Phi_i^{(n-1)*} h(\rho^{(n-1)}, \tau^{(n-1)}, \nabla \cdot \mathbf{J}^{(n-1)}) \Phi_i^{(n-1)}.\tag{1.29}$$

The BCS equations are solved at each iteration with the e_i^n 's to obtain the BCS occupation probability v_i^2 .

The Gram-Schmidt algorithm works as follows,

$$\begin{aligned}\Phi_i &= \tilde{\Phi}_i - \sum_{j=1}^{i-1} (\Phi_j, \tilde{\Phi}_i) \Phi_j, \\ \Phi_i &\rightarrow \frac{1}{\sqrt{(\Phi_i, \Phi_i)}} \Phi_i,\end{aligned}\tag{1.30}$$

where

$$(A, B) = \int A^* B d^3r , \quad (1.31)$$

and the integral is evaluated by the appropriate discretization. Wave functions with different parities and z -signatures are, by definition, already orthogonalized. Therefore it is only necessary to perform the Gram-Schmidt procedure separately in each of the parity and z -signature blocks of the neutron and proton wave functions.

The boundary conditions of the system are chosen so that the wave functions vanish outside the box.

The error of the total binding energies by using a mesh spacing, Δx , of 1fm is about 0.5%. See Ref. [8] for a complete analysis of the error as a function of Δx .

Chapter 2

Implementation on Parallel Computers

2.1 Introduction

The method of solving the HF equations in coordinate space as described in Chapter 1 requires lots of memory and CPU power. It is even more so when one wishes to study the octupole degrees of freedom which are very important for nuclei in the actinide region. In order to obtain the energy surface as a function of octupole deformation, we need to add a octupole constraint field as described in Eq. (1.21) by replacing the Q with octupole operators which breaks the parity symmetry in Eq. (1.9). However, the z -signature symmetry is not broken by the octupole operators. Therefore, the reflection symmetry with respect to $z = 0$ plane in Table 1.1 is broken while the reflection symmetry with respect to $x = 0$ and $y = 0$ planes are still preserved. As a result, we need to solve the HF equation in 1/4th, instead of 1/8th, of the total configuration space. Besides doubling the volume of the mesh, it also doubles the number of overlaps to be calculated for Gram-Schmidt orthonormalization, and thus each overlap takes twice as long to complete. Because of its even more demanding computational resources, we choose to parallelize the

code that allows octupole deformation instead of the one that has the parity symmetry.

We now give an estimate of the computational resources needed to perform such a calculation on ^{208}Pb , and discuss the needed computational speed and memory. We choose a mesh spacing of $\Delta x = 1$ fm and a mesh size of $16(M_x) \times 16(M_y) \times 32(M_z)$ which is big enough for ^{208}Pb so that the boundary effects can be neglected. The number of grids in the z direction is doubled because there is no reflection symmetry with respect to the $z = 0$ plane. For this particular system, we use 90 (N_n) neutron wave functions and 60 (N_p) proton wave functions. The extra ~ 50 wave functions are necessary to allow possible level crossings and pairing.

The memory needed is essentially the memory necessary to store the wave functions and their derivatives. The storage of the derivatives is not absolutely necessary but helps to reduce computation because the derivatives are necessary in both evaluating the HF functional and applying the HF functional to the wave functions. The total storage requirement is thus given by

$$M_x \times M_y \times M_z \times 4 \times (1 + 3) \times (N_p + N_n) \approx 20MW , \quad (2.1)$$

where the factor 4 comes from representing each wave function by 4 real functions and the factor 3 comes from the number of derivatives to be stored. The number of floating point operations (FLOP) needed per iteration can be estimated as

$$M_x \times M_y \times M_z \times (8 \times (N_n^2 + N_p^2) + 500 \times (N_n + N_p)) \approx 1.4(\text{GFLOP}) . \quad (2.2)$$

The number of operations needed to solve the Poisson's equation is independent of the number of wave functions and is small enough that it can be ignored. Orthonormalization accounts for about 58% of the total operations in the ^{208}Pb case and the number of operations grow quadratically with the number of wave functions. In order to reasonably converge the wave functions from Nilsson starting points, at least 200 iterations are

necessary, more if higher precision are required. 280 GFLOP are needed in the ^{208}Pb case for 200 iterations. On a Cray Y/MP, which performs at about 160 MFLOPS with this code, this takes about 30 minutes.

2.2 Decomposition method

There are two obvious ways to decompose the problem on a parallel computer

- Let each node work on only a few of the wave functions. Each node only stores the wave functions it works on.
- Divide the mesh into equal sizes and assign each portion of it to one of the nodes. Each node keeps all the wave functions in that portion of the mesh.

There are two major non-parallelisms in the first method. The first is the calculation of the overlaps in the Gram-Schmidt orthonormalization process. When an overlap between two wave functions kept in different nodes is needed, the wave functions have to be sent from one node to the other in order to compute the overlaps between them. The number of words to be sent can be estimated as

$$\frac{1}{2}n \frac{N_p^2 + N_n^2}{N_p + N_n} M_x M_y M_z \times 4 \approx n(N_p + N_n) M_x M_y M_z, \quad (2.3)$$

where n is the number of processors. The second non-parallelism is the calculation of various densities (ρ , τ and $\nabla \cdot \mathbf{J}$) by combining the partial densities computed in each node which requires $3 \times 2 \times 4 \times M_x M_y M_z$ global sums. Although it takes several times longer to do a global sum than to do a direct exchange, the first non-parallelism will still be the dominant one.

There are three types of non-parallelism involved in the second decomposition method. The first is the calculation of the global overlaps in the orthonormalization process. Each

node first computes a partial overlap from its sub-mesh and the partial overlaps from all the nodes have to be combined. This requires $\approx \frac{1}{2}(N_p^2 + N_n^2)$ global sums. The second is the calculation of derivatives which involves the communication between nodes in charge of neighboring sub-meshes. The dominant ones (those that scales with the number of wave functions) are the calculation of the derivatives of each wave functions and the derivatives of the derivatives of each wave function which is needed when applying Eq. (1.5) to each wave function. Using seven-point formulas, we need to communicate 3 layers deep into the mesh to 6 neighboring nodes for a three-dimensional decomposition. Thus the total exchange volume from these is approximately,

$$(N_p + N_n) \times 2 \times 3 \times (m_x m_y + m_x m_z + m_y m_z) \times 4 \times 2 , \quad (2.4)$$

where m_x, m_y and m_z are the sizes of the sub-mesh in each node which are assumed to be ≥ 3 here. Because of the use of 7-points formula to approximate the derivatives and 9-point formula to approximate the Laplacian, it is more efficient and easier to keep $m_x, m_y, m_z \geq 4$. The final non-parallelism is from solving the Poisson equation when the Laplacian is approximated by a 3 point formula. However, the amount of communications for this is independent of the number of wave functions and can be ignored for more than a few wave functions.

Even though it takes about 20 times longer to do a global sum than to exchange a number between neighboring nodes on DELTA, the second non-parallelism still dominates for any realistic nuclei with even the smallest sub-mesh of $4 \times 4 \times 4$.

For $m_x = m_y = m_z = 8$ which corresponds to a typical $n = 16$ decomposition for our ^{208}Pb case, the first decomposition method needs to communicate $n^2/18 \approx 14$ times more data than the second one. Therefore, the second decomposition method is far superior to the first one in terms of efficiency and it is the one we will use in this research.

The efficiency of our decomposition method is related to the surface to volume ratio of the submeshes as numerical operations are needed to prepare the boundary terms for calculating derivatives in a node. Therefore, it would not be very cost effective to use submeshes smaller than $4 \times 4 \times 4$ even if the communication speed is infinitely fast.

The weak point of our decomposition method is that the maximum number of nodes that the problem can be decomposed to is limited by the total mesh size. Because each node has to have at least $4 \times 4 \times 4$ sub-mesh, the maximum number of nodes we can use is 128 for a total mesh of $16 \times 16 \times 32$.

2.3 Optimizing the communication speed

In order to reduce the communication time, it is very important to take the interconnection topology of the parallel computer into account. Because the major amount of communications in our decomposition method involve communications between nearest neighbor sub-meshes, it is optimal if the nearest neighbor sub-meshes have minimum numbers of communication channels between them.

The 64 nodes in GAMMA are connected as a $2 \times 2 \times 2 \times 2 \times 2 \times 2$ 6-dimensional hypercube. Each node has direct communication channels with its 6 nearest neighbors. Decomposition on GAMMA is very straightforward as it is always possible to have the nearest neighbor sub-meshes assigned to nodes that have direct communication channels. The only consideration here is to reduce the surface of the sub-mesh to reduce the communication volume.

The 512 nodes in DELTA are connected as a 32×16 two-dimensional mesh. Each non-border node has 4 communication channels with its nearest neighbors. Therefore, it is not possible to have all the nearest neighbor sub-meshes assigned to nearest neighbor nodes for a 3-dimensional decomposition. For a $16 \times 16 \times 32$ total mesh, we opt to use 2-dimensional decomposition for $n \leq 32$ instead. For $n \leq 32$, we choose to have the x

direction unsplitted and decompose the y and z direction on DELTA with nearest neighbor sub-meshes assigned nearest neighbor nodes; for $n = 64(8 \times 8)$ or $n = 128(16 \times 8)$, we slice the nodes into four 2×8 or 4×8 node blocks in which the x, z directions are decomposed and the y direction is decomposed onto each of the block. With this decomposition scheme, the nodes assigned to nearest neighbor sub-meshes in x, z directions are connected by direct communication channels while the nodes assigned to nearest neighbor sub-meshes in the y direction are connected by 2 or 4 communication channels for 64 or 128 nodes respectively.

The other consideration is that the overhead for sending a message from one node to the other is very large, therefore it is much more efficient to reduce the number of communication calls by grouping as many messages as possible together and send them as a single message. We accomplished this by copying discontinuous data into a buffer before performing the communication call.

In the original sequential code, the derivatives of the wave functions are stored to save computation time. Because of the limited memory size of each node in GAMMA and DELTA, we find it much more efficient to use this space to store the boundaries of the wave functions in the neighboring sub-meshes. Otherwise, we will need 50% more communication which is much more expensive than recalculating the derivatives.

2.4 Performance and efficiency

The parallel efficiency of a code is defined as

$$\epsilon = \frac{1}{n} \frac{T_{\text{seq}}}{T_n}, \quad (2.5)$$

where n is the number of nodes used, T_n is the time required to complete a calculation in a n -node decomposition and T_{seq} is the corresponding time required for a sequential

code.

For calculations that cannot be performed by sequential code in one node, the important parameter for parallel efficiency is f_C , or fractional communication overhead, defined as

$$f_C = \frac{T_{\text{comm}}}{T_{\text{calc}}} , \quad (2.6)$$

while T_{comm} and T_{calc} are the amount of time in a calculation spent in communication or calculation respectively.

In the optimal case when $T_{\text{calc}} = T_{\text{seq}}/n$, ϵ can be related to f_C as

$$\epsilon = \frac{1}{1 + f_C} , \quad (2.7)$$

and the efficiency will be 1 if T_{comm} or $f_C = 0$. In most cases, however, $T_{\text{calc}} > T_{\text{seq}}/n$ and the efficiency will be less than 1 even if $f_C = 0$. In our case, the number of floating operations needed in each node can be estimated as

$$m_x m_y m_z (8 \times (N_n^2 + N_p^2) + 500 \times (N_n + N_p)) + 100(m_x m_y + m_y m_z + m_x m_z)(N_n + N_p) . \quad (2.8)$$

The operations in the last term are required to calculate the boundary terms for the derivatives. Keep in mind that this estimate is very rough, especially for small submesh or large n where the part of code that does not scale with mesh size becomes important. The Gram-Schmidt operations (first term) have been optimized by using highly optimized i860 assembly language routines. They are very sensitive to the submesh size and run at about 18 MFLOPS when $m_x = m_y = m_z = 16$ and at about 9 MFLOPS when $m_x = m_y = m_z = 4$. The rest of the code only runs at about 4 MFLOPS and also decreases slightly with the decreasing submesh size. Therefore, the efficiency is only expected to be 0.70 for 128 nodes even if $f_C = 0$ in our case.

For the ^{208}Pb calculation described before, the memory requirement of the code de-

mand at least 8 GAMMA nodes and 16 DELTA nodes. More DELTA nodes are needed because there is considerable less memory available to user in each of the DELTA nodes. In order to see how the speed of the code scales with the number of nodes from 1 to 128, we also performed calculations with ^{40}Ca using 20 wave functions. The computational time of these calculations on DELTA, GAMMA and Cray Y/MP are listed in the following tables.

Note that for the ^{40}Ca calculation, T_{calc} 's are reduced by more than two times when the mesh size is reduced by a factor of 2 for $n \leq 8$ on GAMMA and $n \leq 4$ on DELTA. This is probably related to internal CPU caching. The Cray Y/MP runs at about 160 MFLOPS for the ^{208}Pb system and about 111 MFLOPS for the ^{40}Ca system. By using the time T_{calc} , we see that Intel i860 chip performs at about 3.5 – 5.9 MFLOPS for ^{208}Pb system and about 2.0 – 3.5 MFLOPS for the ^{40}Ca system. The large variation of speed is due to that the integer operations are unaccounted for and they become comparable to the floating point operations at small submeshes or large n . The total CPU power of 32 i860 nodes is roughly equivalent to the CPU power of a Cray Y/MP CPU. However, taking the communication overhead into account in this application, we need 64 nodes to match the speed of a Cray Y/MP.

While the T_{calc} 's are reduced by roughly a factor of 2 by doubling n , the T_{comm} 's are reduced by a much less rate. This is because the surface to volume ratio increases and the communication speed decreases due to smaller communication buffer as n increases. As a result, the communication overhead f_C increases with the increasing n .

2.5 Conclusion

Although the DELTA system performs much less than what it was claimed, it is still comparable or faster than the traditional supercomputers. The communication speed of DELTA is barely adequate. Although we could not decompose our code on the whole

Table 2.1: Computational time for 200 iterations of ^{208}Pb

| System | n | Submesh | T_{tot} | T_{calc} | T_{comm} | f_C |
|-----------|-----|--------------------------|------------------|-------------------|-------------------|-------|
| Cray Y/MP | 1 | $16 \times 16 \times 32$ | 28:00 | 28:00 | N.A. | N.A. |
| GAMMA | 8 | $8 \times 8 \times 16$ | 128:03 | 95:12 | 32:51 | 0.34 |
| | 16 | $8 \times 8 \times 8$ | 77:36 | 50:44 | 26:52 | 0.53 |
| | 32 | $8 \times 8 \times 4$ | 52:27 | 32:12 | 20:15 | 0.63 |
| DELTA | 16 | $16 \times 4 \times 8$ | 71:28 | 52:40 | 18:48 | 0.36 |
| | 32 | $16 \times 4 \times 4$ | 46:32 | 32:28 | 14:04 | 0.43 |
| | 64 | $8 \times 4 \times 4$ | 27:52 | 17:26 | 10:26 | 0.60 |
| | 128 | $4 \times 4 \times 4$ | 18:01 | 10:00 | 8:01 | 0.80 |

Table 2.2: Computational time for 200 iterations of ^{40}Ca

| System | n | Submesh | T_{tot} | T_{calc} | T_{comm} | f_C | ϵ |
|-----------|-----------------------|--------------------------|------------------|-------------------|-------------------|-------|------------|
| Cray Y/MP | 1 | $16 \times 16 \times 32$ | 2:45 | 2:45 | N.A. | N.A. | N.A. |
| GAMMA | 1 | $16 \times 16 \times 32$ | 116:00 | 116:00 | 0:00 | 0.00 | 1.00 |
| | 2 | $16 \times 16 \times 16$ | 53:51 | 49:56 | 3:55 | 0.08 | 1.16 |
| | 4 | $16 \times 16 \times 8$ | 28:43 | 22:15 | 6:28 | 0.25 | 1.01 |
| | 8 | $8 \times 8 \times 16$ | 15:34 | 10:42 | 4:52 | 0.45 | 0.93 |
| | 16 | $8 \times 8 \times 8$ | 9:46 | 5:50 | 3:56 | 0.67 | 0.74 |
| | 32 | $8 \times 8 \times 4$ | 6:37 | 3:33 | 3:04 | 0.86 | 0.55 |
| | 64 | $4 \times 4 \times 8$ | 4:24 | 2:03 | 2:21 | 1.15 | 0.41 |
| DELTA | 1 | $16 \times 16 \times 32$ | 110:01 | 110:01 | 0:00 | 0.00 | 1.00 |
| | 2 | $16 \times 16 \times 16$ | 51:26 | 49:16 | 2:10 | 0.04 | 1.07 |
| | 4 | $16 \times 16 \times 8$ | 25:06 | 21:37 | 3:29 | 0.16 | 1.09 |
| | 8 | $16 \times 16 \times 4$ | 14:45 | 11:07 | 3:38 | 0.33 | 0.93 |
| | 16 | $16 \times 4 \times 8$ | 9:06 | 6:13 | 2:53 | 0.46 | 0.75 |
| | 32 | $16 \times 4 \times 4$ | 5:33 | 3:30 | 2:03 | 0.59 | 0.62 |
| | 64 | $8 \times 4 \times 4$ | 3:32 | 2:05 | 1:27 | 0.69 | 0.48 |
| 128 | $4 \times 4 \times 4$ | 2:24 | 1:18 | 1:06 | 0.84 | 0.36 | |

512 nodes in our application, we can still achieve another kind of parallelism by doing simultaneous runs of several different systems in separate partitions. As most HF calculations require calculating many different nuclei at different deformation and/or angular momenta, this proves to be very useful as we can obtain several data points at once. The other advantage of the parallel computing is that not many users are currently using it, therefore it is much easier to get time allocation on it and it has a much better job turn around time than a traditional supercomputer.

The future of parallel computing is still rather promising. The current state-of-the-art CPU chips can outperform Intel i860 by 3-5 times and they keep improving. However, the communication speed has to be sped up by at least that amount to really take advantage of these CPU powers. More and more parallel computers, like CM-5 and Paragon, are being constructed and are going to be available soon.

Chapter 3

Cranked Hartree-Fock Study of Superdeformed Rotational Bands

3.1 Introduction

It is well known that throughout the periodic table, nuclei can adopt a rich variety of shapes, particularly when rotated. This is the result of the interplay between macroscopic (liquid drop) and microscopic (shell correction) contributions to the total energy of the nucleus. Strongly elongated nuclear configurations (with axis ratio larger than 1.5:1) have been predicted some twenty years ago to explain the fission isomers observed in some actinide nuclei. Such phenomenon, usually known as superdeformation (SD), is due to shell effects associated with new “magic” numbers, different from those observed at normal deformation. Such metastable states at 0 spin have indeed been found in the $A = 190$ mass regions, both in HF plus BCS calculations and in Strutinsky-type calculations. It was later realized that such superdeformed shapes can occur at high angular momentum in lighter nuclei with the discovery of a superdeformed band of nineteen discrete lines in ^{152}Dy [14]. The recent discovery of a new “island” of superdeformation in the $A = 190$ mass region with more than 25 SD bands identified at rather low spins (as low as $8\hbar$)

[15] further confirms such predictions.

Among the many striking features found in these SD rotational bands, the most striking one is the recent discovery of pairs of bands with nearly identical deexcitation γ rays energies in nuclei differing by one or two mass units. These bands are commonly referred to as identical bands (IB) or twin bands. In section 3.2, we discuss the experimental backgrounds of identical bands and why they come as a surprise to nuclear theorists.

In this chapter, we try to study such phenomenon using the cranked Hartree-Fock (CHF) method. In section 3.3, we describe CHF method. In section 3.4, we apply CHF method to study the superdeformed identical bands in the Hg region and in section 3.5 we apply the method to the bands in the Dy region. Finally in section 3.6, we draw our conclusions.

3.2 Identical bands

Since the review by Nolan and Twin [16], where the first two SD bands in the $A = 150$ mass region were discussed (^{152}Dy and ^{149}Gd), the “island” of SD nuclei in this mass region has expanded considerably. In the $A = 150$ mass region, ^{152}Dy can be described as a “doubly magic” nucleus: all available calculations indicate the presence of very large shell gaps at $Z = 66$ and $N = 86$ at a quadrupole deformation of $\beta_2 \approx 0.6$.

The discovery of multiple SD bands within a single nucleus has made it possible to investigate the microscopic structure of both the ground and excited states in the second well. However, a greater impetus of detailed studies of excited bands has been the unexpected discovery of several pairs of related bands with almost identical transition energies. The first reported cases [17] consist of the pairs ($^{151}\text{Tb}^*$, ^{152}Dy) and ($^{150}\text{Gd}^*$, ^{151}Tb), the * denotes an excited SD band, where γ -ray transition energies, (E_γ), of the pair were found to be equal to within 1 – 3 keV over a span of 14 transitions with E_γ ranging from

600 keV to 1400 keV. Later, another pair ($^{149}\text{Gd}^*$, ^{150}Tb) was found [18]. This implies that the transition energies are equal to better than 3 parts in a thousand. This is rather surprising as from a simple $A^{5/3}$ rule for quadrupole moments and moments of inertia, we would expect the energy difference to be 14 keV. Furthermore, the spins of corresponding transitions in each pair necessarily differ by $1/2\hbar$, leading to difference in E_γ of ~ 13 keV. For $(A - 1^*, A)$ pairs, with A even, these differences would reinforce each other. A word of caution though, we assume here that each pair of transitions being compared has the appropriate spins $(I + 1/2, I)$, but the spins of the SD bands have not been measured. The spin of the lowest member SD band in ^{152}Dy was estimated to be $22\hbar$.

There are even more examples of identical SD bands in the $A = 190$ mass region [19, 20]. However, two features distinguish the bands in this region from those near $A = 150$:

- many of the identical bands occur in pairs separated by two mass units,
- a large number of bands can be related to the SD band in ^{192}Hg , which appears to serve as a doubly-magic core in this region.

Only one SD band has been observed in ^{192}Hg [21, 22]. Bands with γ -rays identical to those of ^{192}Hg haven been seen in ^{194}Pb [23, 24, 25] and in ^{194}Hg [26, 27]. Only one band has been found in ^{194}Pb ; its γ -rays have identical energies with those of ^{192}Hg to better than a couple of keV over angular momentum ranging from 12 to $30\hbar$. Three bands were observed in ^{194}Hg , one of which, labeled the second excited band or band 3, also “twins” with the same ^{192}Hg band for 15 consecutive transitions.

Since the unexpected discovery of SD twinned bands, it has been shown [28, 29, 30] that such twinned bands had already been found in the rare-earth and the actinide region at normal deformation, though this was not explicitly pointed out in the original analysis of the data.

The puzzle comes partly from the fact that many theoretical models include an in-

trinsic scaling with mass. In models based on oscillators, the volume conservation law depends upon the mass number. Similarly, the Strutinsky method relies partly on a liquid drop formula. Despite these uncertainties, detailed analyses using parametrized mean fields have been performed. Dudek *et al.* [32] were able to derive analytical expressions for the contributions of each single particle orbitals to the moment of inertia within the rotating oscillator model. Ragnarsson [31] studied the contribution to the moment of inertia due to the alignment of valence particle using either modified oscillator or Woods Saxon single particle wave functions. Both studies arrive at the conclusions that the contribution to the moment of inertia of the single particle orbitals depends very much both on deformation and on the Nilsson quantum numbers of the orbitals, some orbitals bringing nearly no contributions to the moment of inertia. Another attempt to explain this phenomenon [33] relies on the strong coupling limit of the particle rotor model. Again, the filling of specific orbitals favors the appearance of identical bands in nuclei differing by one mass unit. This last result assumes that the moment of inertia of the even-even core is not affected by the extra particle, an hypothesis which is not easy to justify.

Our goal is to check the above ideas within a parameter free model. Furthermore, we want to see whether this twinning phenomenon is within the scope of a mean field description of superdeformation. For that purpose, a method based neither on a scaling law nor on an inert core assumption is necessary. The cranked Hartree-Fock method (CHF) with Skyrme like interactions meets these two requirements. Indeed, its sole ingredient, the effective interaction, is not specially designed to fit the properties of SD states; it does not make any use of scaling law and no inert core approximation is made. Within this spirit, Girod *et al.* [34] have constructed three SD bands in ^{192}Hg , two of them being nearly identical. However variation of the mean field with rotation was not included in their model. Therefore, this calculation was limited to low angular momentum (below $22\hbar$) for the sole ^{192}Hg nucleus where only one SD band has been observed.

3.3 Cranked Hartree-Fock method

The cranking approximation is based on the assumption that a nucleus with spin J can be described in terms of an intrinsic state at rest in a frame rotating with some angular velocity ω around an axis. The optimal intrinsic state $|\Psi\rangle$ is determined by minimization of the Routhian \mathcal{E}

$$\mathcal{E} = E - \omega J_z , \quad (3.1)$$

where E and J_z are respectively the expectation values of the Hamiltonian and of the third component of the angular momentum

$$J_z = \langle \Psi | \hat{J}_z | \Psi \rangle . \quad (3.2)$$

The angular velocity ω which acts as a Lagrange multiplier is determined by the condition

$$J_z = J . \quad (3.3)$$

In this work E is calculated within the HF+BCS approximation as described in Chapter 1, using a functional derived from a Skyrme interaction.

Because of the breaking of the time-reversal symmetry by the operator \hat{J}_z , the local Hamiltonian density can no longer be given by the simple formula of Eq. (1.5). When the spin degrees of freedom are taken into account, the breaking of time reversal symmetry leads to a rather complicated functional [35, 36]. The local Hamiltonian density can be expressed as,

$$\begin{aligned} \mathcal{H}(\mathbf{r}) = & \frac{\hbar^2}{2m} \tau + B_1 \rho^2 + B_2 (\rho_n^2 + \rho_p^2) + B_3 (\rho \tau - \mathbf{j}^2) + B_4 (\rho_n \tau_n - \mathbf{j}_n^2 + \rho_p \tau_p - \mathbf{j}_p^2) \\ & + B_5 \rho \Delta \rho + B_6 (\rho_n \Delta \rho_n + \rho_p \Delta \rho_p) + B_7 \rho^{2+\alpha} + B_8 \rho^\alpha (\rho_n^2 + \rho_p^2) \end{aligned}$$

$$\begin{aligned}
& +B_9(\rho\nabla\cdot\mathbf{J}+\mathbf{j}\cdot\nabla\times\rho+\rho_n\nabla\cdot\mathbf{J}_n+\mathbf{j}_n\cdot\nabla\times\rho_n+\rho_p\nabla\cdot\mathbf{J}_p+\mathbf{j}_p\cdot\nabla\times\rho_p) \\
& +B_{10}\rho^2+B_{11}(\rho_n^2+\rho_p^2)+B_{12}\rho^\alpha\rho^2+B_{13}\rho^\alpha(\rho_n^2+\rho_p^2)+E_C.
\end{aligned} \tag{3.4}$$

The mass densities ρ_q , kinetic density τ_q and spin-orbit density $\nabla\cdot\mathbf{J}_q$ are given in Eq. (1.8), while the current density \mathbf{j}_q and the vector density $\rho_q(q=n,p)$ are given by

$$\begin{aligned}
\mathbf{j}(\mathbf{r}) &= \frac{1}{2}i\sum_{k\sigma}v_k^2(\Phi_k^*(\mathbf{r},\sigma)\nabla\Phi_k(\mathbf{r},\sigma)-\Phi_k(\mathbf{r},\sigma)\nabla\Phi_k^*(\mathbf{r},\sigma)), \\
\rho(\mathbf{r}) &= \sum_{k\sigma\sigma'}v_k^2\Phi_k^*(\mathbf{r},\sigma)\Phi_k(\mathbf{r},\sigma')\langle\sigma|\sigma|\sigma'\rangle.
\end{aligned} \tag{3.5}$$

The coefficients $B_{i=1-9}$ are given in Eq. (1.6), the rest can be expressed as,

$$\begin{aligned}
B_9 &= \frac{1}{2}W, & B_{12} &= \frac{1}{24}t_3x_3, \\
B_{10} &= \frac{1}{4}t_0x_0, & B_{13} &= -\frac{1}{24}t_3, \\
B_{11} &= -\frac{1}{4}t_0.
\end{aligned} \tag{3.6}$$

We impose the same parity, Eq. (1.9), and z -signature, Eq. (1.10), symmetries on the individual wave functions. Because of breaking of the time-reversal symmetry, we have to solve the HF equations for both members of the signature partners.

The HF equation (1.14) becomes

$$\begin{aligned}
h'\Phi_i(\mathbf{r},\sigma) &= \sum_{\sigma'}\left\{-\nabla\frac{\hbar^2}{2m_q^*(\mathbf{r})}\nabla\delta_{\sigma\sigma'}+U_q(\mathbf{r})\delta_{\sigma\sigma'}+\mathbf{V}_q(\mathbf{r})\cdot\langle\sigma|\sigma|\sigma'\rangle\right. \\
&\quad \left.+i\mathbf{C}_q(\mathbf{r})\cdot\nabla\delta_{\sigma\sigma'}+i\mathbf{W}_q(\mathbf{r})\cdot(\langle\sigma|\sigma|\sigma'\rangle\times\nabla)\right\}\Phi_i(\mathbf{r},\sigma'),
\end{aligned} \tag{3.7}$$

where h' is the single-particle Routhian $h'=h-\omega\hat{J}_z$. The effective mass m_q^* and spin-orbit \mathbf{W}_q are the same as in Eq. (1.15), while the spin scalar U_q , spin vector \mathbf{V}_q , and current \mathbf{C}_q are given by

$$U_q(\mathbf{r}) = 2B_1\rho+2B_2\rho_q+B_3(\tau+i\nabla\cdot\mathbf{j})+B_4(\tau_q+i\nabla\cdot\mathbf{j}_q)$$

$$\begin{aligned}
& +2B_5\Delta\rho + 2B_6\Delta\rho_q + (2 + \alpha)B_7\rho^{1+\alpha} \\
& +B_8(\alpha\rho^{\alpha-1}\sum_q\rho_q^2 + 2\rho^\alpha\rho_q) + B_9(\nabla\cdot\mathbf{J} + \nabla\cdot\mathbf{J}_q) \\
& +\alpha\rho^{\alpha-1}(B_{12}\rho^2 + B_{13}(\rho_n^2 + \rho_p^2)) + \delta_{q,+1/2}V_C(\mathbf{r}) , \\
\mathbf{V}_q & = B_9(\nabla\times\mathbf{j} + \nabla\times\mathbf{j}_q) + 2B_{10}\rho + 2B_{11}\rho_q + 2\rho^\alpha(B_{12}\rho + B_{13}\rho_q) - \frac{1}{2}\hbar\omega\mathbf{e}_z , \\
\mathbf{C}_q & = 2B_3\mathbf{j} + 2B_4\mathbf{j}_q - B_9(\nabla\times\rho + \nabla\times\rho_q) + \hbar\omega(\mathbf{e}_z\times\mathbf{r}) . \tag{3.8}
\end{aligned}$$

For a rotating nucleus the time reserved state $\Phi_{\bar{i}}$ of Φ_i is no longer an eigenstate of the Routhian h' . Because of this, we could no longer describe pairing using the simple BCS formalism as in section 1.3.3. To properly describe pairing, we have to use the Hartree-Fock-Bogoliubov (HFB) method. However, the method of solving HFB equations using Skyrme force in coordinate spaces has been only developed recently and is very numerically intensive.

In this work, we choose to ignore the pairing correlations completely. For SD rotational bands in the Dy region, the lowest spin is larger than $20\hbar$ and it is believed that pairing force is substantially weakened at such high spin and thus it can be ignored. However, because SD rotational bands in the Hg region start from $8\hbar$, the pairing correlation can't be completely ignored. It has been shown that the variation of the moment of inertia of SD bands with spin is certainly related to the gradual disappearance of pairing correlation with rotation. However, we do not believe that pairing is responsible for the very existence of twinned bands. Moreover, the strength of the pairing force is not well known at such large deformations: calculations based on a Woods-Saxon potential and a seniority pairing interaction require an *ad hoc* renormalisation of the pairing strength in order to reproduce the experimental increase of the dynamical moment of inertia \mathcal{J}_2 [27]. Finally, pairing is known not to affect in a significant manner the bulk of the mean field, especially near shell closure. We expect that pairing will not change the basics of the mean field shape of ^{192}Hg which is magic when superdeformed, so that the resulting

single particle orbitals will remain unchanged.

Our cranked HF code has also been transposed onto the massively parallel Intel DELTA and GAMMA computers as described in Chapter 2. All the calculations described here have been performed on the DELTA.

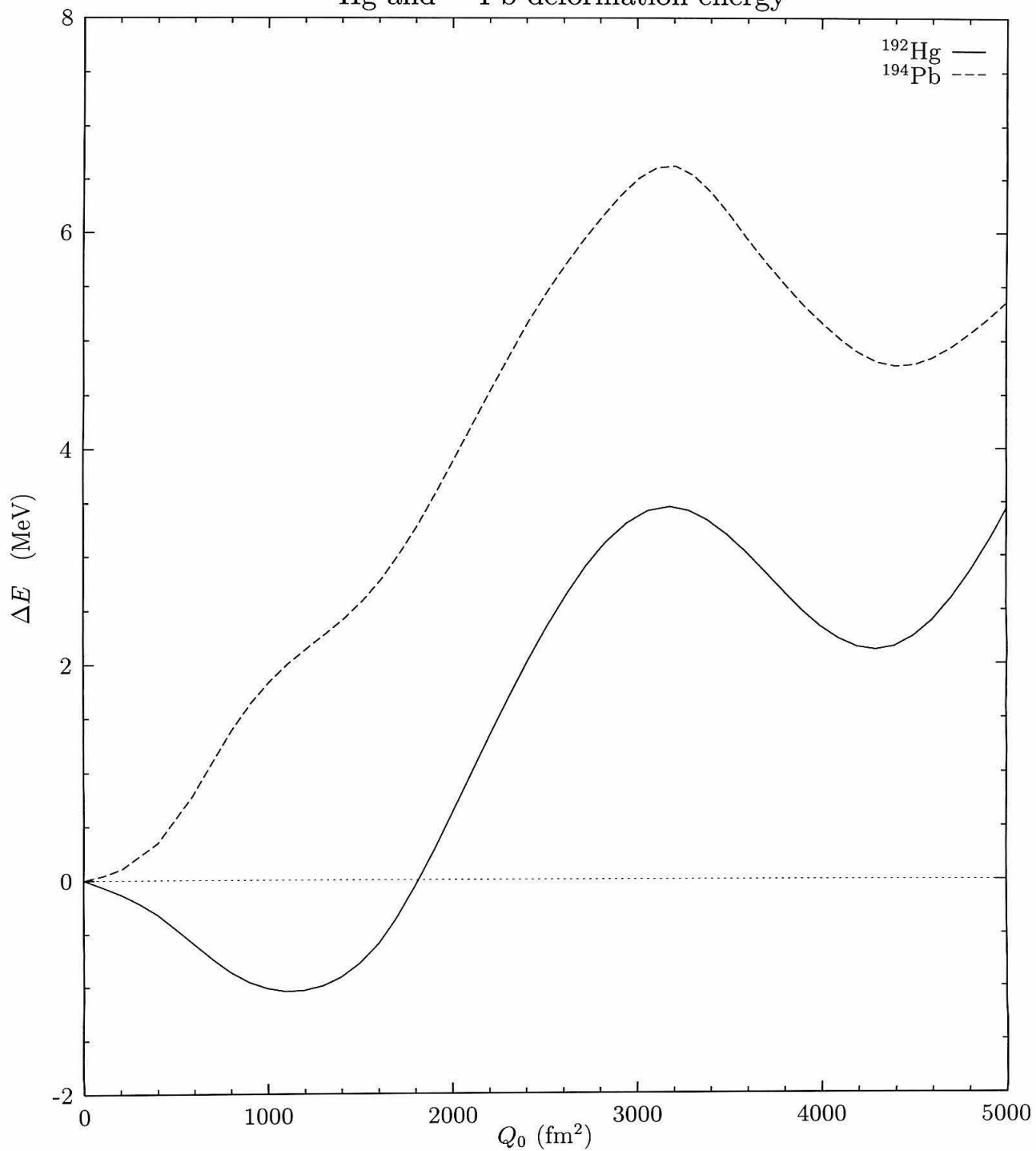
3.4 Identical SD Bands in $A = 190$ mass region

We choose to study the SD bands in the $A = 190$ regions first because in this region of the mass table bands twinned with the SD band of the “magic” SD nucleus ^{192}Hg have been detected in two even-even nuclei: ^{194}Hg [26, 27] and ^{194}Pb [23, 24, 25]. Thus we avoid the complications and ambiguities intrinsic to odd nuclei.

Fig. 3.1 shows the deformation energy curve of ^{192}Hg and ^{194}Pb at 0-spin with pairing. ^{194}Pb has a spherical ground state while ^{192}Hg has a deformed ground state. However, both nuclei have secondary superdeformed minima at about 4400 fm^2 which correspond to the axis ratio of about 1.6 : 1.

The SD ground state rotational bands are built by cranking on the 0-spin superdeformed minima without pairing. The excited bands are built by introducing blockings on the single particle occupations to excite one or more nucleons to some excited orbitals.

Fig. 3.2 shows the neutron and proton Routhians for ^{192}Hg SD ground-state band as a function of J_z . Nilsson quantum numbers have been tentatively assigned to some relevant orbitals. As discussed by Meyer *et al.* [37], HF orbitals are a mixture of many different Nilsson orbitals so that this identification is only a means to compare with other works. Most orbitals do not display large signature splitting and their Routhians are essentially independent of J_z . A few intruder orbitals are rapidly down-sloping, but not in the range of angular momentum of interest. The Routhian of these orbitals behave similarly to those obtained in Ref. [27] using a Woods-Saxon potential. However, the neutron gap at $N = 112$ is much less pronounced in our calculation.

^{192}Hg and ^{194}Pb deformation energyFigure 3.1: Deformation energy curve for ^{192}Hg and ^{194}Pb at 0-spin with pairing

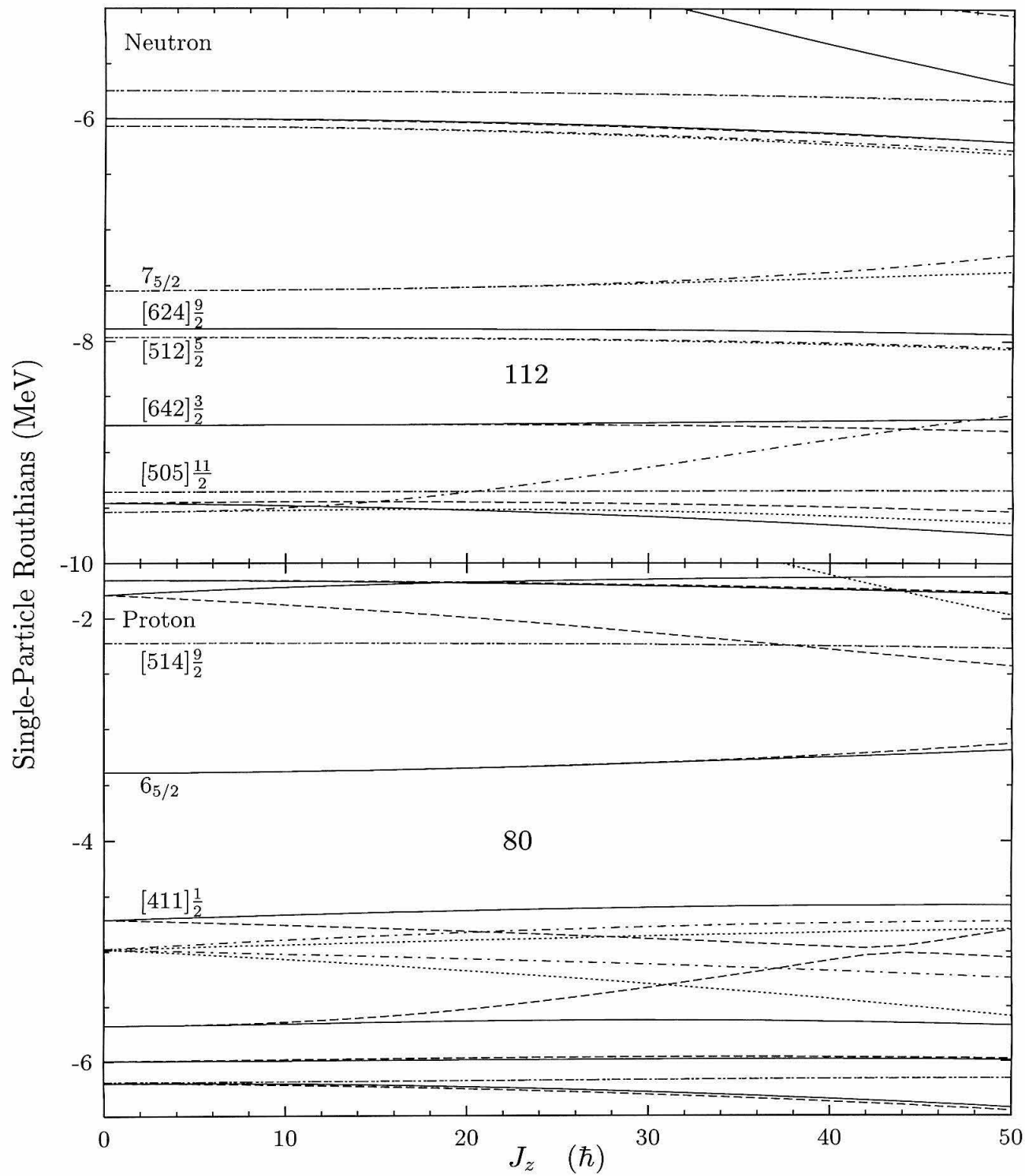


Figure 3.2: Neutron and proton Routhians for ^{192}Hg . The parity and signature (P,S) of each individual orbitals are indicated by solid (+,+), dashed (+,-), dot-dashed (-,+) and dotted (-,-) lines.

Table 3.1: Energies, quadrupole moments, dynamical \mathcal{J}_2 and rigid body moments of inertia \mathcal{J}_0 and angular frequencies ω obtained at $20\hbar$ for the five SD bands studied in this work

| Band | E (MeV) | E_{rot} (MeV) | Q_0 (fm ²) | \mathcal{J}_2 (MeV ⁻¹) | \mathcal{J}_{rig} (MeV ⁻¹) | ω (MeV) |
|----------------------|-----------|------------------------|--------------------------|--------------------------------------|---|----------------|
| ¹⁹² Hg | -1507.734 | 1.74468 | 4446.009 | 115.407 | 119.319 | 0.17392 |
| ¹⁹⁴ Pb | -1513.777 | 1.81887 | 4644.611 | 110.681 | 122.365 | 0.18151 |
| ¹⁹⁴ Pb(*) | -1511.611 | 1.73897 | 4383.145 | 116.009 | 120.133 | 0.17318 |
| ¹⁹⁴ Hg | -1523.683 | 1.71442 | 4393.146 | 117.925 | 120.300 | 0.17056 |
| ¹⁹⁴ Hg(*) | -1523.350 | 1.73655 | 4446.266 | 116.279 | 120.709 | 0.17285 |

We have constructed two ¹⁹⁴Pb bands, which we will refer to as ¹⁹⁴Pb and ¹⁹⁴Pb(*) by filling either the $6\frac{5}{2}$ or the $[514]\frac{9}{2}$ proton orbitals. Similarly, we have calculated two ¹⁹⁴Hg bands referred to as ¹⁹⁴Hg and ¹⁹⁴Hg(*) by filling either the $[512]\frac{5}{2}$ or the $[624]\frac{9}{2}$ neutron orbitals. All five bands have $K = 0$. Table 3.1 summarizes our results at $20\hbar$ for these five bands. The dynamical moments of inertia, \mathcal{J}_2 , are calculated as $\frac{dJ_z}{d\omega}$. The excitation energy of the ¹⁹⁴Pb(*) band relative to the ¹⁹⁴Pb band is 2.6MeV, while it is only 0.33MeV for the ¹⁹⁴Hg(*) band.

The excitation energies for these five bands versus J_z are shown in fig. 3.3. They are drawn relative to a rigid-body reference so that comparison is easier. Three of the bands (¹⁹²Hg, ¹⁹⁴Pb(*) and ¹⁹⁴Hg(*) have a remarkably close behavior, contrary to the ¹⁹⁴Pb and ¹⁹⁴Hg bands. The correspondence between the two bands ¹⁹⁴Hg(*) and ¹⁹⁴Pb(*) is even more striking. These two nuclei have the same mass number; no scaling law is expected. Further comparison with the ¹⁹²Hg band, which is two mass units away shows that this global law plays no role on such a small mass difference. To support the interpretation of these bands as identical, or twinned, bands, we have plotted the differences in γ ray energies between the $A = 194$ bands and the ¹⁹²Hg one taken as a reference in Fig. 3.4. Such a plot requires an unusual accuracy in the CHF calculation. We have checked that we have actually reached an accuracy of the order of a few tenths of keV on the γ ray

energy differences. Another consistency check of the quality of our results is the very smooth behavior of all the energy differences with respect to angular momentum. The four bands show deviations with respect to the ^{192}Hg reference proportional to J_z . For both ^{194}Pb and ^{194}Hg nuclei, the deexcitation energies of their excited bands differ by 1–3 keV from that of ^{192}Hg over the experimentally observed range of angular momentum. Our calculation predicts that these differences may be somewhat larger at higher angular momenta, say above $32\hbar$. The other bands in ^{194}Pb and ^{194}Hg do not resemble each other at all. Neither of them twins with the ^{192}Hg band.

Fig. 3.5 shows the dynamical moments of inertia \mathcal{J}_2 as a function of J_z for the five SD bands calculated by differentiating the total angular momentum with respect to ω . Such a calculation leads to larger numerical inaccuracies than the differences in γ ray energies, which are responsible for the not completely smooth behavior of \mathcal{J}_2 . Despite these numerical uncertainties, this plot supports the conclusion that the $^{194}\text{Hg}^{(*)}$ and $^{194}\text{Pb}^{(*)}$ bands are identical to each other and to that of ^{192}Hg , whereas no such conclusion can be drawn for the two other bands. Again, deviations are more pronounced for the higher angular momentum reported on the figure. For the lowest transitions, the moment of inertia of the ^{192}Hg band and of the two identical $^{194}\text{Hg}^{(*)}$ and $^{194}\text{Pb}^{(*)}$ are equal to better than 3 parts in a thousand, which is even smaller than what is extracted from experiment. The overall trends of these moments are quite similar except that the two excited bands display slightly larger \mathcal{J}_2 slopes than the three SD ground-state bands. All five bands display a continuous rise of \mathcal{J}_2 with the increasing angular momentum.

Experimentally the dynamical moments of inertia \mathcal{J}_2 of ^{192}Hg increases from $90 \hbar^2\text{MeV}^{-1}$ at band head to about $140 \hbar^2\text{MeV}^{-1}$ at angular momentum of about $42 \hbar$. Other bands in this region behave similarly, except that they have not been detected at such high angular momentum. Wood-Saxson [38] and rotating oscillator [31] calculations without pairing generate a mean field in a way which leads to moment of inertia independent of angular velocity. By introducing pairing and renormalizing the neutron and

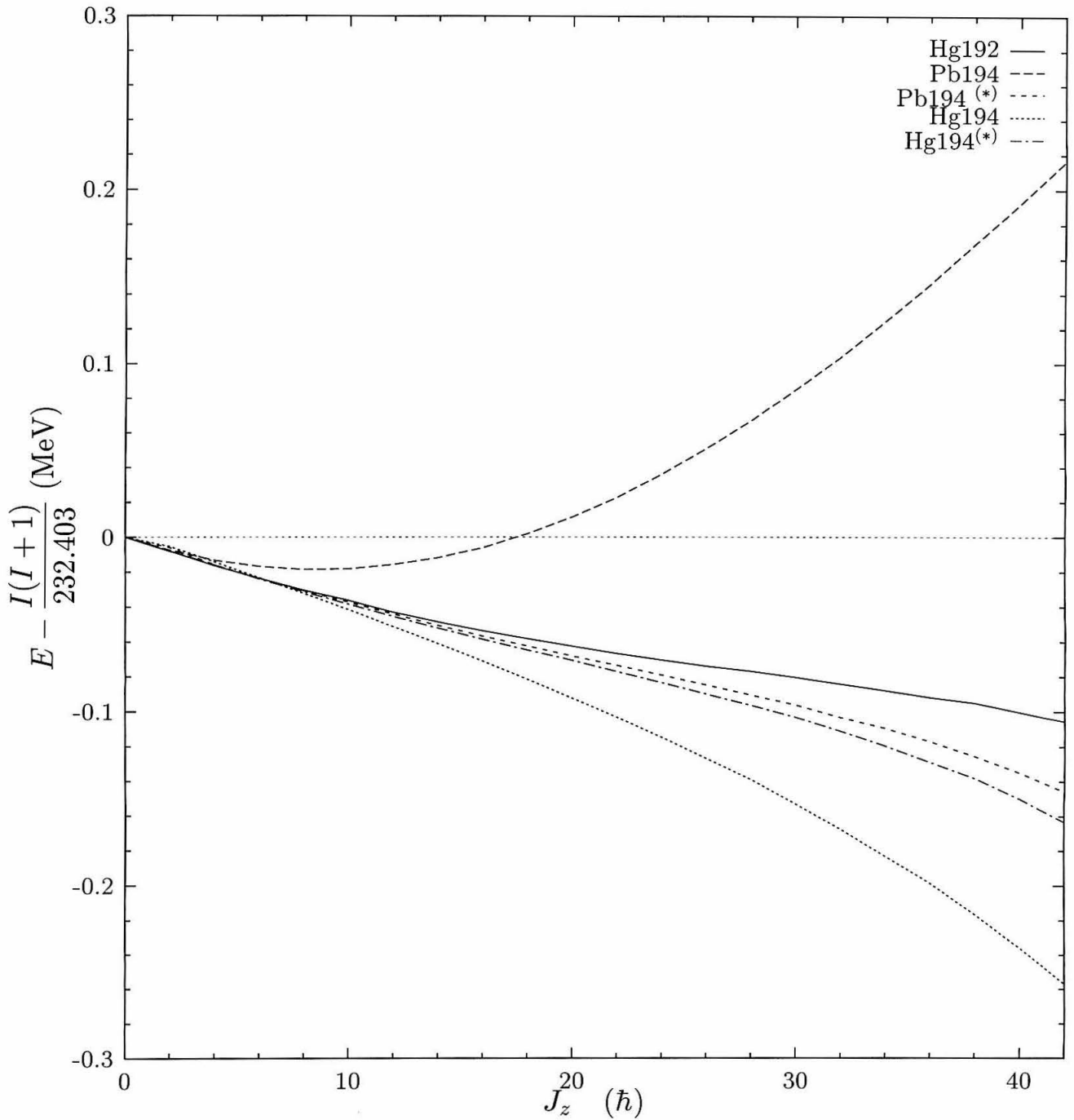


Figure 3.3: Rotational energies (relative to a rigid rotor reference) vs. spin for the various bands constructed here. The band-head energies have been subtracted.

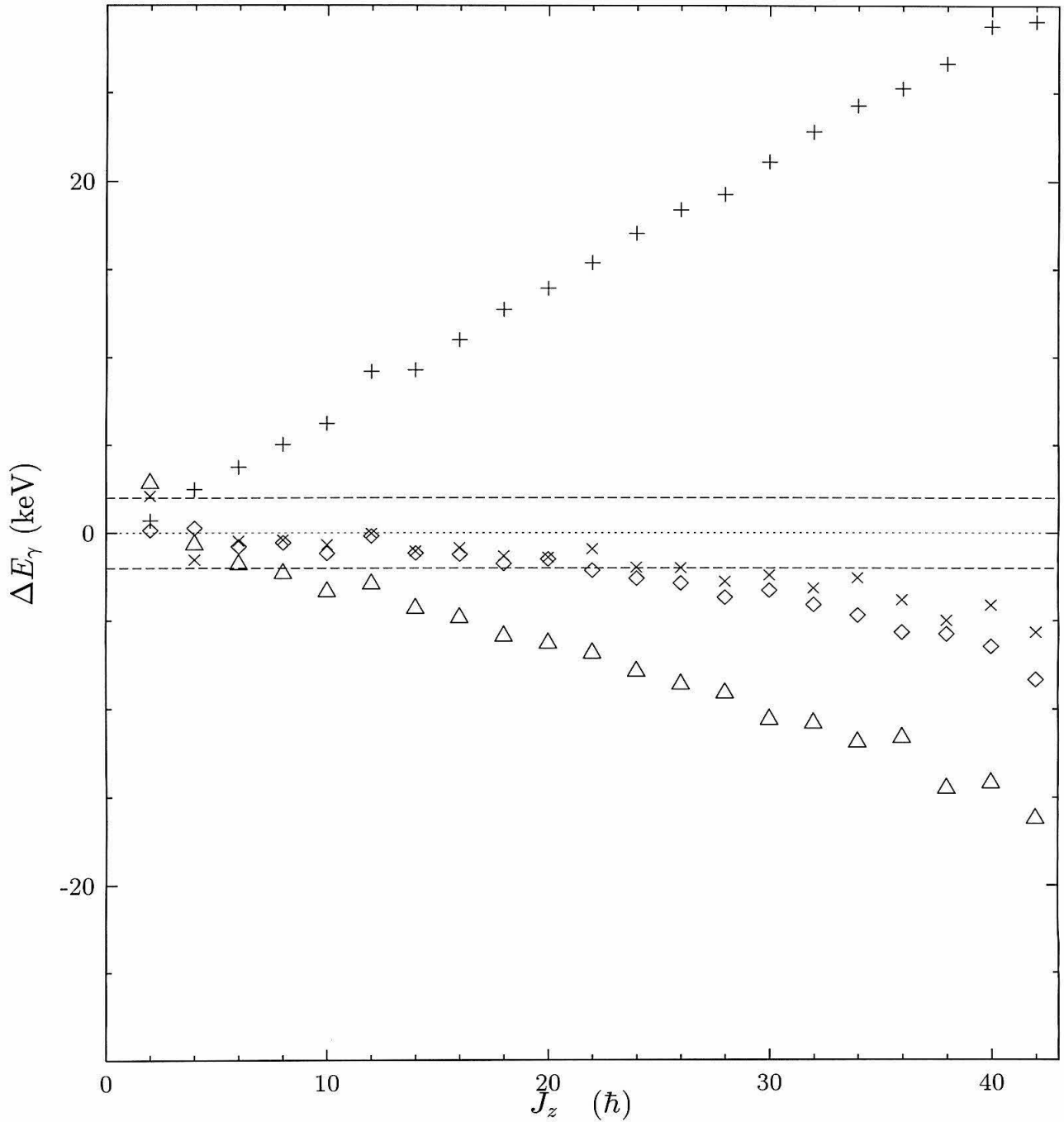


Figure 3.4: Differences in γ ray energies ΔE_γ between the $A = 194$ bands and the ^{192}Hg band. The bands are represented by $+$ (^{194}Pb), \times ($^{194}\text{Pb}^{(*)}$), Δ (^{194}Hg), and \diamond ($^{194}\text{Hg}^{(*)}$). The two dashed lines at ± 2 keV represent the accuracy required experimentally for twinning.

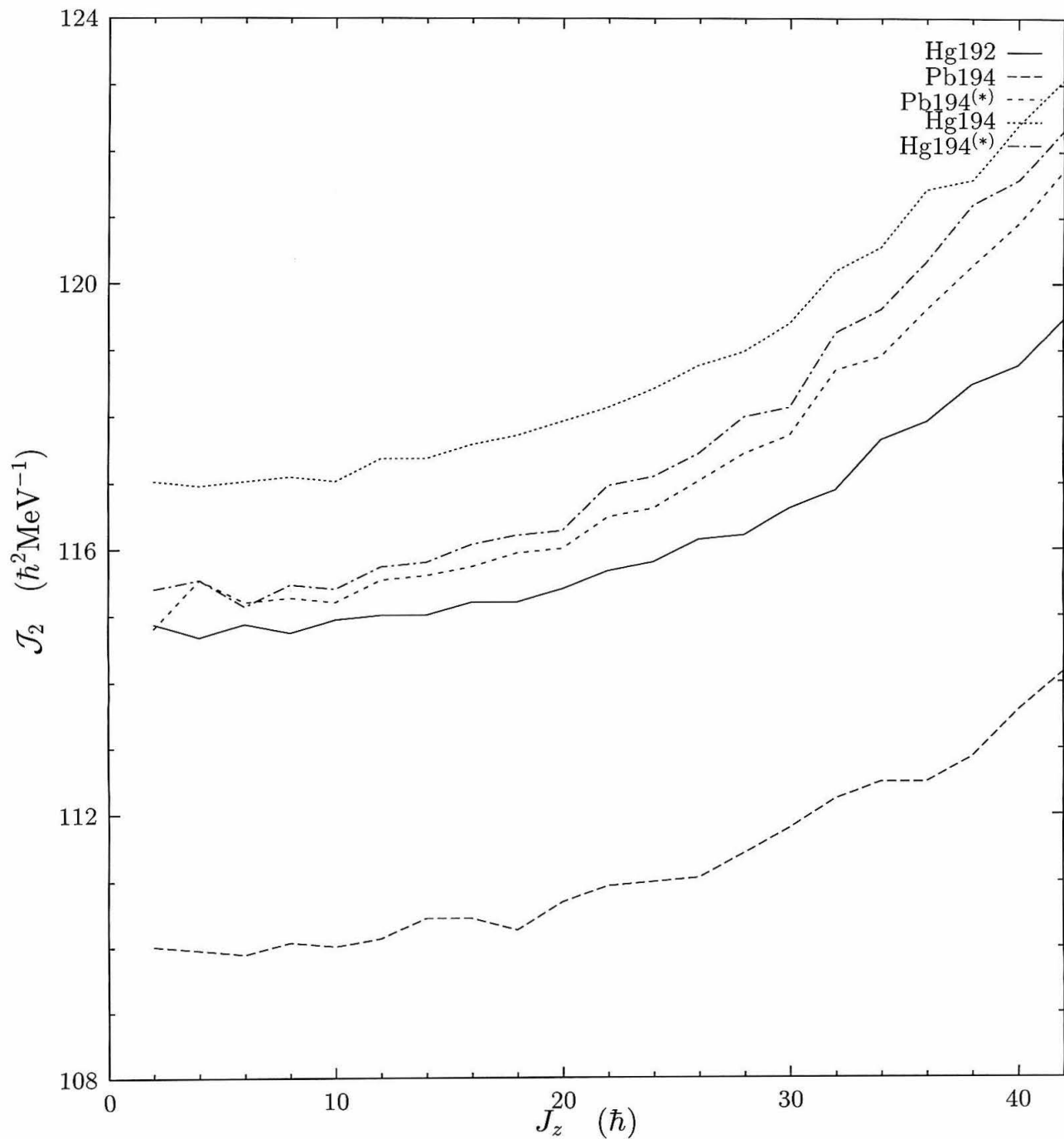


Figure 3.5: Dynamical moments of inertia \mathcal{J}_2 for the five bands constructed.

proton pairing strengths, Strutinsky calculations can reproduce the experimental slope of \mathcal{J}_2 for $J_z \leq 32\hbar$ at which point the calculated \mathcal{J}_2 reaches a maximum and starts to decrease while the experimental \mathcal{J}_2 keeps increasing[27].

Our results contradict these other studies in that all five bands display continuous rise of \mathcal{J}_2 with the increasing angular momentum in the angular momentum range of interest, although much less pronounced than the experimental ones due to the lack of pairing. Further calculations show that the \mathcal{J}_2 does not start to decrease until $J_z = 52\hbar$.

A first possible explanation of our results could be that the different behaviors observed for the four $A = 194$ bands are related to some properties of the single particle orbitals added to the ^{192}Hg core. We have to first look whether the effect of the single particle orbitals on \mathcal{J}_2 is correlated to a similar effect on deformation. The quadrupole moments of the five bands are given in Fig. 3.6. They remain essentially constant as a function of J_z , exhibiting a slight decrease with the increasing angular momentum nearly independent of band. This feature is in agreement with the experimental measurements of transition quadrupole moments Q_t [39]. Table 3.1 shows that the overall changes in the quadrupole moments from one band to the other are not related to the changes in dynamical moments of inertia. The ^{194}Pb band has a larger quadrupole moment and a smaller moment of inertia, while the situation is inverted for the ^{194}Hg band. These features illustrate that neither the dynamical moments of inertia nor the quadrupole moments obey the $A^{5/3}$ rule. Indeed, as expected, the relative values of the rigid body moments of inertia follow the same trends as the quadrupole moments. They are all significantly different from the \mathcal{J}_2 values, the largest differences being obtained for the ^{194}Pb SD ground-state band.

To understand the origin of twinning, it is important to examine how the two extra particles added to the ^{192}Hg core contribute to the rotation. Table 3.2 shows the single-particle Routhian energies at $20\hbar$ and $40\hbar$ for the eight orbitals filled in the various bands we have constructed here together with their single-particle contributions to the

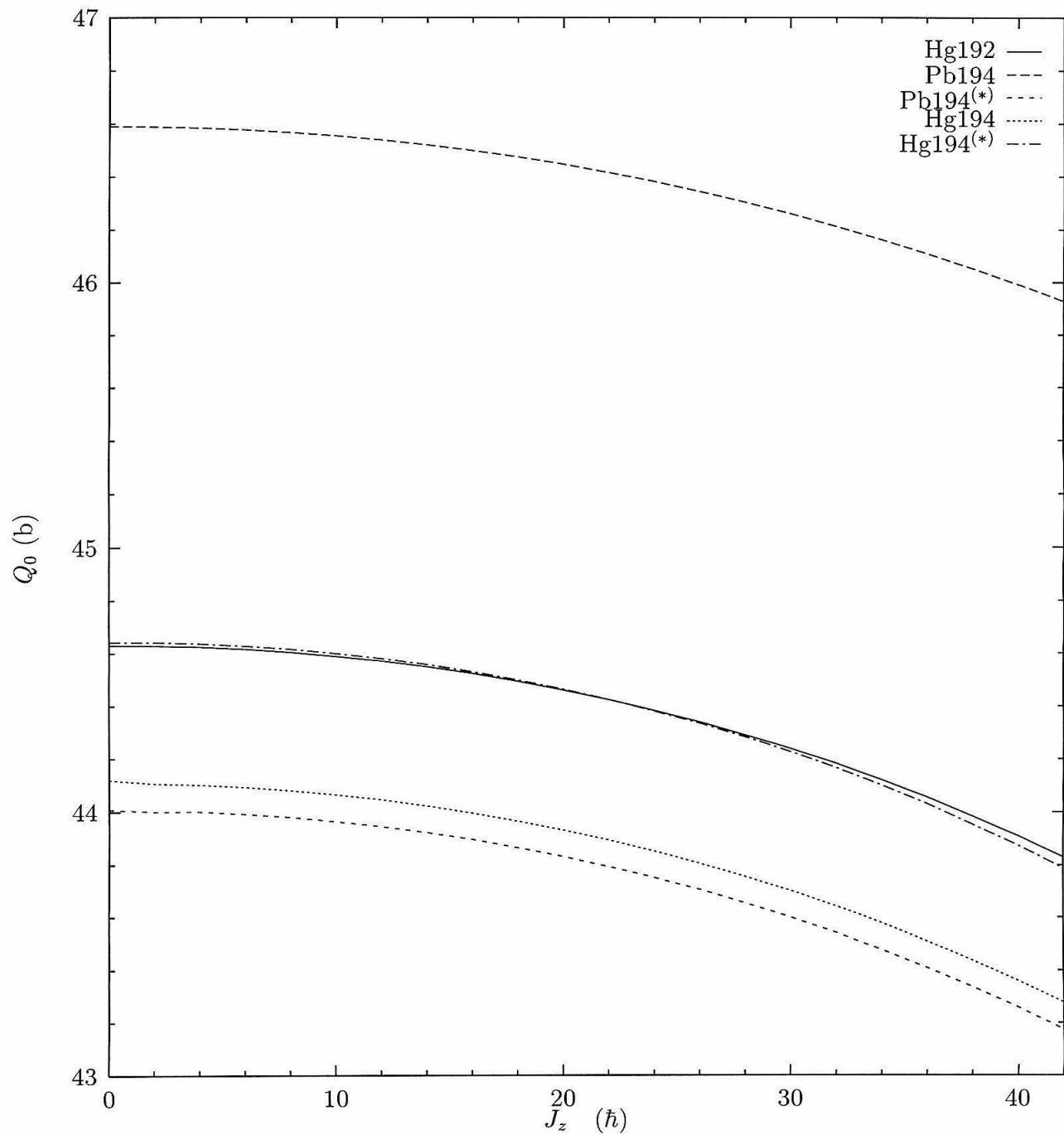


Figure 3.6: Quadrupole moment as a function of J_z for all the bands constructed here.

Table 3.2: Angular momenta j_z , contributions to \mathcal{J}_2 and single-particle Routhian energies of the eight orbitals added to the ^{192}Hg orbitals

| | ^{194}Pb | | $^{194}\text{Pb}^{(*)}$ | | ^{194}Hg | | $^{194}\text{Hg}^{(*)}$ | |
|------------------------|-------------------|-------------|-------------------------|------------------|-------------------|------------------|-------------------------|------------------|
| | $6_{5/2}^+$ | $6_{5/2}^-$ | $[514]_{2}^{9+}$ | $[514]_{2}^{9-}$ | $[512]_{2}^{5+}$ | $[512]_{2}^{5-}$ | $[624]_{2}^{9+}$ | $[624]_{2}^{9-}$ |
| $20\hbar j_z$ | -0.241 | -0.260 | -0.174 | -0.175 | -0.077 | -0.049 | -0.165 | -0.164 |
| $\frac{dj_z}{d\omega}$ | -1.247 | -1.739 | -1.013 | -1.014 | -0.373 | -0.331 | -0.993 | -0.993 |
| ϵ_{sp} | -2.927 | -2.927 | -1.870 | -1.870 | -8.120 | -8.125 | -7.989 | -7.989 |
| $40\hbar j_z$ | -0.357 | -0.625 | -0.349 | -0.350 | -0.130 | -0.105 | -0.345 | -0.344 |
| $\frac{dj_z}{d\omega}$ | -0.062 | -2.148 | -1.048 | -1.054 | -0.322 | -0.310 | -1.129 | -1.124 |
| ϵ_{sp} | -2.821 | -2.798 | -1.883 | -1.883 | -8.173 | -8.184 | -8.103 | -8.103 |

angular momentum J_z and to \mathcal{J}_2 . This last contribution is calculated as $\frac{dj_z}{d\omega}$. These orbitals show small signature splitting, especially the ones leading to identical bands. They have negative alignments along the rotational axis and negative contributions to the moment of inertia. The extra orbitals filled in $^{194}\text{Hg}^{(*)}$ and $^{194}\text{Pb}^{(*)}$ bring very similar contributions to the moment of inertia. Although small, these negative contributions are not negligible, they represent 1.5% of the total angular momentum. The extra orbitals of ^{194}Pb have more negative angular momenta and contributions to \mathcal{J}_2 , leading to a lower dynamical moment of inertia than in ^{192}Hg , while the situation is reversed for ^{194}Hg . In this last case, the extra two particles bring very small contributions to the angular momentum and to the moment of inertia, but do not lead to twinning. This indicates that the core polarization of ^{192}Hg induced by the added particles is by no mean negligible. “Twinning” thus results from a delicate balance between the contribution of the extra particles and the self-consistent response of the mean field.

The tiny variation of the single particle Routhians with rotational frequency indicates that the single-particle angular momenta are not equal to the derivatives of the single-particle Routhians with respect to the rotational frequency, as they are if the mean field

Hamiltonian does not depend on ω . We have verified this by taking the derivatives of the Routhians, which leads to values of j_z smaller by at least a factor 5 than those obtained from the mean values. This shows that the main contribution to the single particle angular momenta is coming from the variation of the mean field with angular momentum. This variation has two origins. The first is the dependence of the nuclear deformation on rotation. Such dependence is also included in calculations based on parametrized mean fields and leads to very small effects. The second effect is dominant in our calculation and is due to terms appearing in microscopically determined mean fields when time reversal invariance is broken. These terms arise from the velocity dependent terms of the effective interaction and are of the order of 1 MeV at $40\hbar$.

From the observation that the dependence of the mean field on the angular velocity ω is a key ingredient to obtain twinning, one can ask whether **full** self consistency is also necessary. For that purpose, we have calculated the energies and angular momenta of the various ^{194}Pb and ^{194}Hg bands at 0, 20 and $40\hbar$, describing each of their states by the appropriate filling of the ^{192}Hg orbitals, without further self consistency. The ^{192}Hg orbitals, however, are the results of fully self-consistent and converged HF calculations carried out at each angular momentum. The angular momenta of the ^{194}Pb and ^{194}Hg states obtained from that of ^{192}Hg (from table 1) and the contribution of the two extra orbits (from table 2) are smaller than the angular momentum of the ^{192}Hg core. However, when both the energy and the angular momenta are estimated to the same first-order, the corresponding points in an energy- J_z plane lie almost exactly on the fully self-consistent curve for each SD bands. Moreover, the first order, or nonself-consistently, γ ray energies of the four bands approximate the fully self-consistent ones with an accuracy better than 1%. This unexpected feature shows that the crucial point to obtain twinning is a correct calculation of the rate of variation of the single particle angular momenta and of the Routhians as a function of ω .

Our results present some similarity with those obtained by Ragnarsson [31] and by

Dudek [32], who have also shown that the filling of specific single-particle orbitals lead to twinning. However, our calculation points out the importance of the dependence of the mean field on the rotation, an effect not included in previous calculations. In our study, twinning does result from a precise balance between the changes of the mean field and the behavior of single-particle states.

Let us summarize some of the common properties of single particle orbitals that lead to twinning:

- They are oblate shape driving orbitals as opposed to intruder or prolate shape driving orbitals.
- They have nearly no signature partner splitting.
- They all have a small but similar amount of anti-alignment along the rotation axis.

3.5 Identical SD Bands in $A = 150$ mass region

The nucleus ^{152}Dy is generally regarded as the doubly “magic” nucleus in this region. Only one excited SD band in ^{151}Tb is found to twin with the ^{152}Dy band. Therefore, we have to deal with an odd- A nucleus here which is much more complicated.

^{152}Dy has a spherical ground state and instead of having a SD secondary minimum, it has a SD shoulder. A SD minimum develops from the shoulder when pairing is turned off and the SD rotational band can be constructed from that minimum.

Fig. 3.7 shows the neutron and proton Routhians of the ^{152}Dy SD rotational band. As expected, there are large neutron and proton shell gaps at 86 and 66 respectively.

By invoking the pseudo SU(3) symmetry, previous models based on strong coupling limit assign the quasi particle configuration of the $^{151}\text{Tb}^*$, the twin band of ^{152}Dy , to be $A \otimes \pi([301]_{\frac{1}{2}})^{-1}$ [33, 40]. The $[301]_{\frac{1}{2}}$ orbitals are chosen because under pseudo SU(3) scheme, their pseudo-spin is aligned along the rotational axis with $\tilde{s} = \pm\frac{1}{2}$ which leads

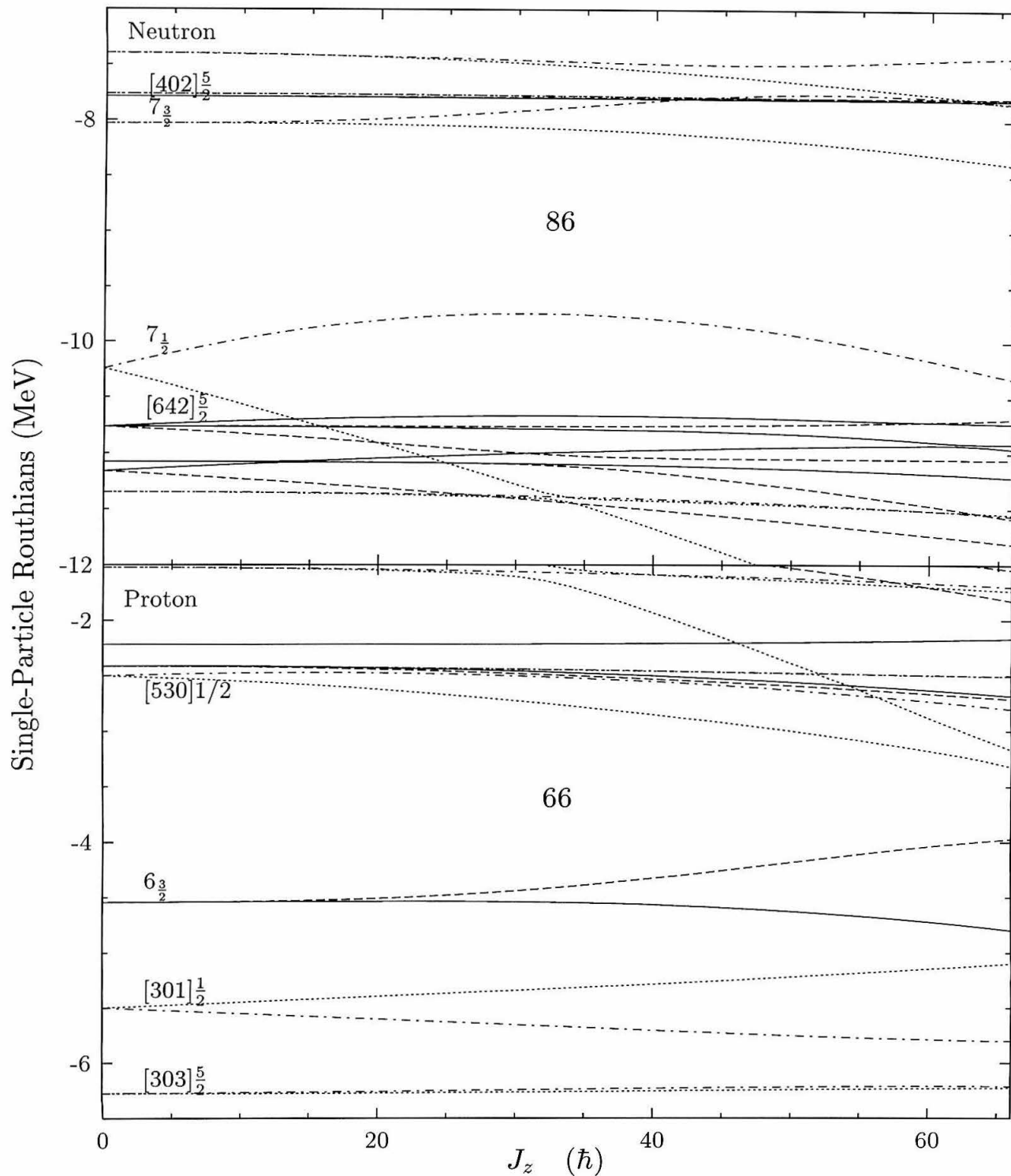


Figure 3.7: Neutron and proton Routhians for ^{152}Dy . The parity and signature (P,S) of each individual orbitals are indicated by solid (+,+), dashed (+,-), dot-dashed (-,+), and dotted (-,-) lines.

to twinning between an even-even core and its neighboring odd- A nucleus under strong coupling limit if the moments of inertia of the two are identical[41]. However, the $[301]_{\frac{1}{2}}$ orbitals do not fit the criteria for orbitals leading to twinning found in the previous section as they have large signature splittings and one of the orbitals has positive alignment along the rotational axis. The $\pi[303]_{\frac{5}{2}}$ orbitals, however, appear to be much better candidates based on our previous findings.

We constructed three ^{152}Tb bands which we will refer to as $^{151}\text{Tb}^*$, $^{151}\text{Tb}^\dagger$ and $^{151}\text{Tb}^{\dagger\dagger}$ by emptying the orbitals $[301]_{\frac{1}{2}}^-$, $[303]_{\frac{5}{2}}^+$ and $[303]_{\frac{5}{2}}^-$ bands respectively. We only consider the $[301]_{\frac{1}{2}}^-$ orbital here because it is the orbital that is assigned by pseudo SU(3) symmetry that leads to twinning and it is interesting to see if we can observe some kind of pseudo spin alignment in the Hartree-Fock method.

Fig. 3.8 shows the dynamical moments of inertial of these three bands together with the ^{152}Dy band. Contrary to the Hg region, the \mathcal{J}_2 's here decrease continuously when $J_z \geq 20$. The experimental \mathcal{J}_2 of ^{152}Dy is also found to decrease with slopes similar to what we have here, although their absolute values are about 5% less. The better agreement between the HF and the experimental \mathcal{J}_2 here is not surprising because pairing does not play an important role in the SD bands in this region. The two $K = \pm\frac{5}{2}$ bands have the \mathcal{J}_2 remarkably close to that of ^{152}Dy aside from a few wiggles due to numerical inaccuracy. The \mathcal{J}_2 of these two bands are equal to that of ^{152}Dy well within the experimental accuracy. The $K = \frac{1}{2}$ band shows several times larger the difference in \mathcal{J}_2 . This is in agreement with the results of the previous section as both the $K = \pm\frac{5}{2}$ bands have about the same amount of negative alignment as those orbitals which lead to twinning in ^{194}Pb and ^{194}Hg while the $K = \frac{1}{2}$ orbital has a too negative alignment leading $^{151}\text{Tb}^*$ to have a too large \mathcal{J}_2 . Numerically, the j_z of the three orbitals emptied in band $^{151}\text{Tb}^*$, $^{151}\text{Tb}^\dagger$ and $^{151}\text{Tb}^{\dagger\dagger}$ at $20 \hbar$ are -0.31 , -0.18 and $-0.16 \hbar$ respectively. The j_z of $[301]_{\frac{1}{2}}^-$ orbital varies from $-0.26 \hbar$ at J_z of $10.5 \hbar$ to $-0.42 \hbar$ at J_z of $60.5 \hbar$, while the j_z of the other two orbitals increase almost linearly with J_z . No quantized alignment

of $-0.5 \hbar$ suggested by pseudo SU(3) is observed here.

The comparison of E_γ between the ^{152}Dy band and the odd A bands is somewhat complicated by the fact that $K \neq 0$ for the odd A bands and the simple cranking model formula $I = \sqrt{\langle \hat{J}_x^2 \rangle + \langle \hat{J}_z^2 \rangle}$ is very likely not valid at high spin. The condition that I being half integer for odd- A nucleus can't be simply translated to that J_z has to be half integer at high spin. Because $[301]1/2^-$ orbital has a more or less constant alignment near -0.5 at high angular momentum, we choose to compare E_γ between $^{151}\text{Tb}^*$ and ^{152}Dy at J_z pairs of $(J_z + \frac{1}{2}, J_z)$. Since the other two bands have the alignment more or less proportional to J_z , we choose to compare their E_γ with that of ^{152}Dy 's at the same J_z . Fig. 3.9 shows the difference between the E_γ 's of the three ^{151}Tb bands with that of the ^{152}Dy band. Such a plot suggests that all three of the Tb rotational bands can be considered identical to the ^{152}Dy band at $J_z \leq 40\hbar$. However, the band $^{151}\text{Tb}^*$ shows deviation proportional to J_z , and the twinning disappears when $J_z \geq 40\hbar$. On the other hand, the other two bands have the deviations always smaller than 3 keV in the angular momentum of interest. The only difference between the two bands being that the $^{151}\text{Tb}^\dagger$ band has a sizable deviation at low angular momentum while the deviation in $^{151}\text{Tb}^\ddagger$ grows with J_z at low angular momentum. One should note that if the E_γ of the $^{151}\text{Tb}^*$ band is compared to that of ^{152}Dy at pairs of the same J_z , these two bands could not be considered twinning at all.

Other possible configurations in constructing ^{151}Tb are also explored, however, none of them appears to be a good candidate for twinning after calculations of a few points.

As discussed above, it appears acceptable by assigning the experimental ^{151}Tb twin band to be either one of the three configurations considered here. Our calculations suggest it is more favorable for the twin band to be either of the $K = \pm\frac{5}{2}$ bands instead of the $K = 1/2$ band as suggested by pseudo SU(3). Because of the nearly zero signature splitting of the $[303]_{\frac{5}{2}}$ orbitals as opposed to the sizable signature splitting of the $[301]_{\frac{1}{2}}$ orbitals, the experimental evidence for supporting the $K = \pm\frac{5}{2}$ band will be that the

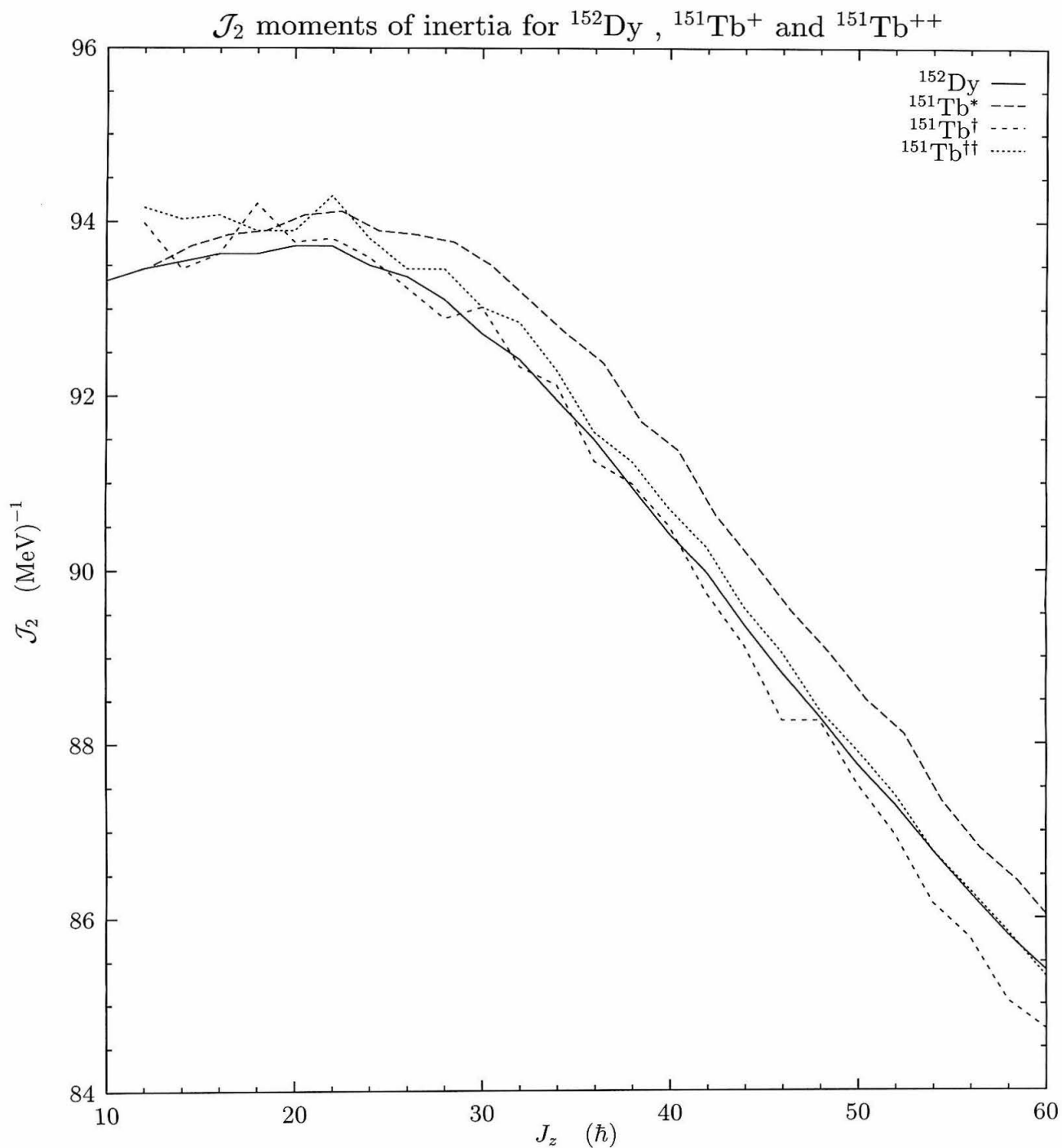


Figure 3.8: Dynamical moments of inertia \mathcal{J}_2 for the ^{151}Tb and ^{152}Dy bands.

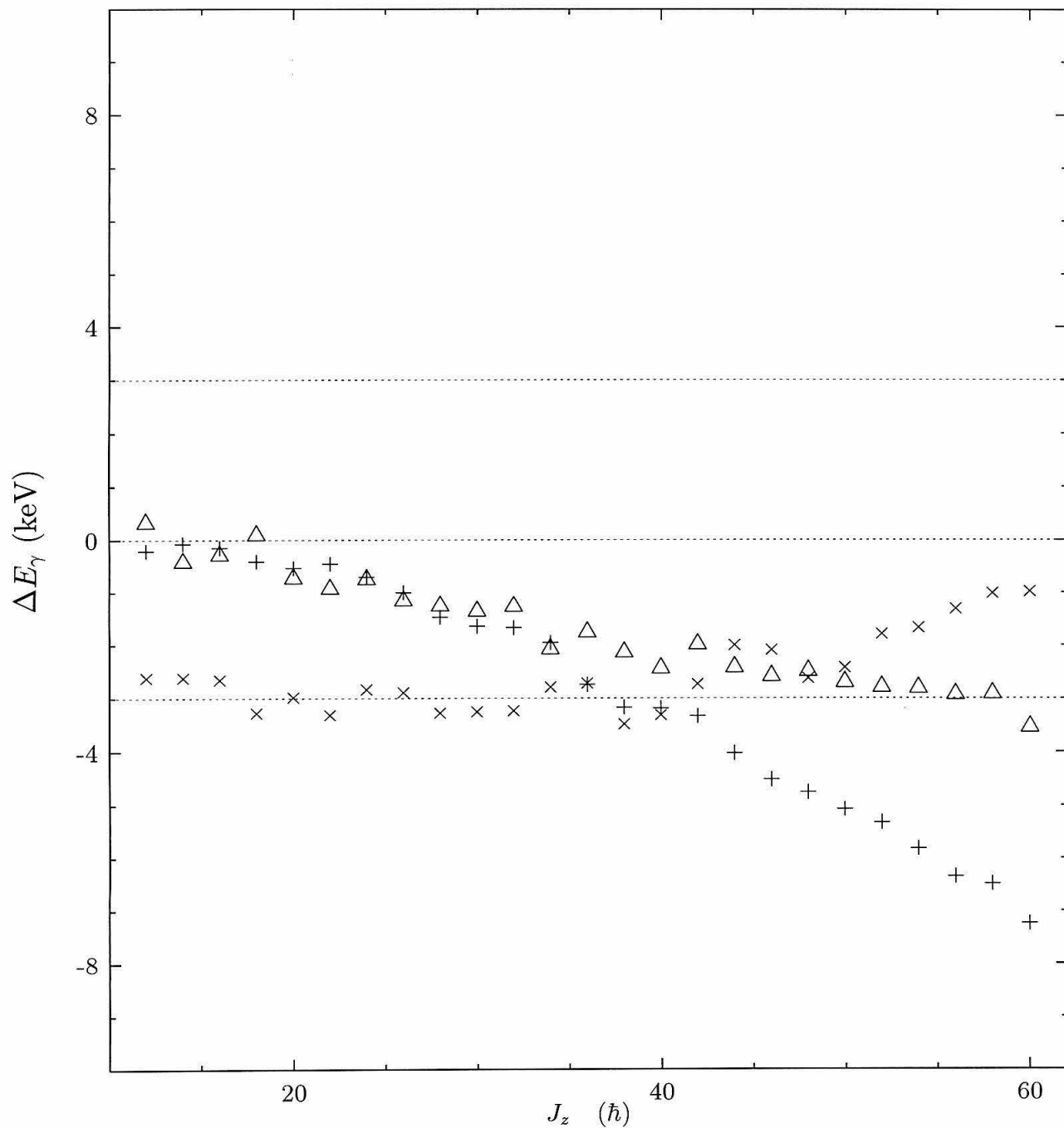


Figure 3.9: Differences in γ ray energies ΔE_γ between the ^{151}Tb bands and the ^{152}Dy band. The bands are represented by + ($^{151}\text{Tb}^*$), x ($^{151}\text{Tb}^\dagger$), Δ ($^{151}\text{Tb}^{\dagger\dagger}$) two dashed lines at ± 3 keV represent the accuracy required experimentally for twinning.

twin band consists of two nearly degenerate bands instead of a single band.

3.6 Conclusion

Let us summarize the results of our calculations.

- Within a fully self-consistent CHF, the filling of specific orbitals leads to identical bands in both the Hg and the Dy regions with an accuracy well within the experimental data.
- Changes of deformation with increasing mass are not simply related to changes in the dynamical moment of inertia. No simple relationship emerges from their comparison.
- Scaling of the moment of inertia by a $A^{5/3}$ rule is not correct for adding or removing a few nucleons. The generality of this rule must be re-examined. In practical applications, when one compares results obtained for neighboring nuclei, this rule is invalidated by single particle effects. Increase in the mass can even lead to decrease in \mathcal{J}_2 , depending on the properties of the single-particle orbitals.
- The correct calculation single particle properties (especially the alignment) is a key ingredient for twinning.

Many features remain to be explained and demonstrated. Most important is to show that pairing will not invalidate the conclusions drawn from this simple CHF picture. The answer to this question will necessitate the introduction of a pairing force with non constant matrix elements between the orbitals. Another important question is the choice of orbitals to construct the SD bands in both the Hg region and the Dy region. *Lastly*, one should note that the one SD band observed in ^{194}Pb twins both experimentally and theoretically to the only band observed in ^{192}Hg . In ^{192}Hg , our calculated band is the

SD band built upon the shape isomer, or SD minimum, whereas in ^{194}Pb it is an excited band. This raises several questions. Although the single particle level schemes calculated with the Skyrme interaction SkM* and with the most frequently used Woods Saxon parametrization are very similar [20], is the quadrupole deformation at which the $6\frac{1}{2}$ and $[514]\frac{9}{2}$ states crosses underestimated? The inclusion of a seniority pairing interaction, although decreasing the quadrupole deformations of the SD bands, does not modify the order of the ^{194}Pb single particle orbitals, at least at zero spin. Assuming the validity of our calculations, is it possible that the SD band built upon the ^{194}Pb SD minimum has not yet been observed? This would question the assumption frequently made by experimenters that the most intense band observed is the lowest one.

Although we have demonstrated that twinning arises within fully self-consistent CHF calculations without further assumptions, there still exists the question: is there a hidden symmetry?

Chapter 4

Atomic parity nonconservation and neutron radii in cesium isotopes

4.1 Introduction

Precision studies of electroweak phenomena provide very important tests of the $SU(2)_L \times U(1)$ Standard Electroweak Model. The measurement of the parity nonconserving (PNC) components of the atomic transitions belongs to this class. It offers a unique opportunity for testing the electroweak radiative corrections at the one-loop level and, possibly, to search for new physics beyond the standard model [42, 43].

The PNC effects in atoms are caused by the γ, Z^0 interference in the electron-nucleus interaction. The dominant contribution comes from the coupling of the axial electronic current to the vector nuclear current. (The interaction of the electronic vector current with the nuclear axial current is weaker in heavy atoms, and can be eliminated by summing over the PNC effects in the resolved hyperfine components of the atomic transitions. The hyperfine-dependent effect, which also includes the nuclear anapole moment, is of interest in its own right [44, 45], but is not considered hereafter.) Since the vector current is conserved, atomic PNC essentially measures the electroweak coupling of the elementary

quarks.

At the present time, PNC measurement in stable ^{133}Cs atoms have $\pm 2\%$ experimental uncertainty [46]. (An earlier experiment in Cs was performed by Bouchiat *et al.* [47]; the studies of PNC effects in atoms have been reviewed by Commins [48] and Telegdi [49].) However, improvement by an order of magnitude in the experimental accuracy is anticipated and a possibility of measuring PNC effects in unstable cesium and francium isotopes has been discussed [50]. At this level, two issues must be resolved before an interpretation of the PNC data in terms of the fundamental electroweak couplings is possible. The atomic theory, even in its presently most sophisticated form [51, 52], introduces about $\pm 1\%$ uncertainty. Moreover, the small but non-negligible effects of nuclear size [53, 54] must be addressed. This latter problem is the main topic of the present work.

Atomic PNC is governed by the effective bound electron-nucleus interaction (when taking only the part that remains after averaging over the hyperfine components) of the form

$$H_{PNC} = \frac{G_F}{2\sqrt{2}} \int [-N\rho_n(\mathbf{r}) + Z(1 - 4\sin^2\theta_W)\rho_p(\mathbf{r})] \times \psi_e^\dagger \gamma_5 \psi_e d^3r, \quad (4.1)$$

where the proton and neutron densities $\rho_{p,n}(\mathbf{r})$ are normalized to unity, and we have assumed the Standard Model nucleon couplings

$$C_{1p} \equiv 2C_{1u} + C_{1d} = \frac{1}{2}(1 - 4\sin^2\theta_W), \quad (4.2)$$

$$C_{1n} \equiv C_{1d} + 2C_{1u} = -\frac{1}{2}. \quad (4.3)$$

The electron part in Eq. (4.1) can be parametrized as [53, 54]

$$\rho_5(r) \equiv \psi_p^\dagger \gamma_5 \psi_s = C(Z)\mathcal{N}(Z, R)f(r), \quad (4.4)$$

where $C(Z)$ contains all atomic structure effects for a point nucleus, \mathcal{N} is a precisely

calculable normalization factor, and $f(r)$ describes the spatial variation (normalized such that $f(0) = 1$). It is the integrals

$$q_{n,p} = \int f(r) \rho_{p,n}(\mathbf{r}) d^3r \quad (4.5)$$

that determine the effect of the proton and neutron distributions on the PNC observables.

The form factors $f(r)$ can be calculated to the order $(Z\alpha)^2$ for a sharp nuclear surface of radius R , and neglecting the electron mass in comparison with the nuclear Coulomb potential [53, 54],

$$f(r) \simeq 1 - \frac{1}{2}(Z\alpha)^2[(r/R)^2 - \frac{1}{5}(r/R)^4 + \frac{1}{75}(r/R)^6] . \quad (4.6)$$

For accurate calculations numerical evaluation of $f(r)$ is necessary (see below). However, the coefficients at $\langle r^2 \rangle$ and $\langle r^4 \rangle$ remain numerically of the order $(Z\alpha)^2$ and depend only weakly on the exact shape of $\rho_{p,n}(\mathbf{r})$. In addition, since the electric potential near the nucleus is very strong, one can safely neglect atomic binding energies in the evaluation of $f(r)$ (but not the electron mass). Below we will separate the effects of the finite nuclear size (i.e., effects related to the deviations of $q_{n,p}$ from unity); these terms will be represented by a nuclear structure correction to the weak charge.

Taking the matrix element of H_{PNC} , one obtains

$$\langle i | H_{PNC} | j \rangle = \frac{G_F}{2\sqrt{2}} C(Z) \mathcal{N} [Q_W(N, Z) + Q_W^{nuc}(N, Z)] , \quad (4.7)$$

where $Q_W(N, Z)$, the quantity of primary interest from the point of view of testing the Standard Model, is the “weak charge”. In the Standard Model, with couplings (4.2) and (4.3), the weak charge is

$$Q_W = -N + Z(1 - 4 \sin^2 \theta_W) . \quad (4.8)$$

The nuclear structure correction $Q_W^{nuc}(N, Z)$ describes the part of the PNC effect that is caused by the finite nuclear size. In the same approximation as Eq. (4.8) above

$$Q_W^{nuc} = -N(q_n - 1) + Z(1 - 4 \sin^2 \theta_W)(q_p - 1), \quad (4.9)$$

where $q_{n,p}$ are the integrals of $f(r)$ defined above. (Nuclear structure also affects the normalization factor \mathcal{N} , which is, however, determined by the known nuclear charge distribution [53, 54].)

In a measurement that involves several isotopes of the same element, ratios of the PNC effects depend essentially only on the ratio of the weak charges and the corresponding nuclear-structure corrections $Q_W(N, Z) + Q_W^{nuc}(N, Z)$. (The dependence \mathcal{N} on the neutron number N will not be considered here.) The ratios of the nuclear-structure corrected weak charges, in turn, depend, to a good approximation, only on the *differences* Δq_n of the neutron distributions in the corresponding isotopes. The uncertainties in these quantities, or equivalently, in the differences of the neutron mean square radii $\delta(\Delta \langle r^2 \rangle_{N, N'})$, then ultimately limit the accuracy with which the fundamental parameters, such as $\sin^2 \theta_W$, can be determined.

It is the purpose of this work to evaluate quantities $q_{n,p}$ for a number of cesium isotopes, which might be used in future high-precision PNC experiments [50]. Moreover, we estimate the uncertainty in these quantities, respectively, in their differences, since they represent the ultimate limitations for the interpretation of the PNC measurements.

In section 4.2, we briefly describe the features of the Hartree-Fock calculations used here. In section 4.3 we compare the calculated binding energies, ground state spins and charge radii of cesium with the experiment. There we also discuss how corrections for the zero-point vibrational motion can be estimated and added. From the spread between the results obtained with two different successful effective Skyrme forces, and from the pattern of deviations between the calculated and measured isotope shifts in the

charge radii, we then estimate the uncertainties in the corresponding differences of the neutron radii. Finally, in section IV, we calculate the nuclear-structure corrections to the weak charges $Q_W^{nuc}(Z = 55, N = 72 - 84)$, and their uncertainties and discuss the corresponding limiting uncertainties in the determination of the fundamental parameters of the Standard Model. (Our notation follows that of Ref. [54]. Others, e.g., Ref. [51] do not explicitly separate the nuclear structure dependent effects. We believe that such a separation is very useful, since, as stated above, $f(r)$ in Eq. (4.6) and hence also $q_{n,p}$, Eq. (4.5), are essentially independent of atomic structure.)

4.2 Nuclear Hartree-Fock calculations

Because we are dealing with odd-A nuclei here, the unpaired nucleon introduces terms that break time-reversal symmetry in the HF functional. Thus, we have to use the CHF method as described in Chapter 3 here.

However, as we are dealing with ground state properties, we cannot simply ignore the pairing as we did in Chapter 3. Fortunately, we can still describe the pairing by the simple BCS formalism because the time-reversal breaking terms in the functional generated by the unpaired odd nucleon are very small compared to the time-reversal conserving terms so that the time reversal symmetry is still approximately good. In the following we define the pairing partner $\Phi_{\hat{k}}$ of state Φ_k to be the eigenstate of h whose overlap with $\hat{T}\Phi_k$ is maximal (\hat{T} is the time-reversal operator). Because the single particle orbital occupied by the unpaired nucleon and its signature partner do not contribute to the pairing energy, we introduce blocking in our code to prevent these two orbitals from participating in pairing and force their BCS occupation numbers to be 1 and 0, respectively.

In the following calculations, the protons and neutrons BCS pairing strengths are chosen to be $17.5/(11 + Z)$ MeV and $16.5/(11 + N)$ MeV respectively. Although the pairing strengths do affect the binding energies, they have little influence on the neutron

or proton radii.

As some of cesium isotopes considered here are deformed, it is very important to take the deformation degrees of freedom into account. The method of solving the HF+BCS equations by discretization of the wave functions on a rectangular mesh allows any type of even multipole deformation. We obtain the deformation energy curve by using the method described in section 1.3.4.

4.3 Comparison with experiment

In Fig. 4.1 we show the deformation energy curves for ^{125}Cs – ^{139}Cs . According to our calculations with SkyrmeIII (SIII) and SkyrmeM* (SkM*) forces the lighter cesium isotopes $N \leq 76$ are deformed. For SIII such an assignment is able to explain the observed ground state spins of $\frac{1}{2}^+$ for $N = 70 - 74$ and $\frac{5}{2}^+$ for $N = 76$. For SkM* the mean field proton states $g_{7/2}$ and $d_{5/2}$ are interchanged and therefore the ground state spin assignments for the deformed cesium isotopes are not correct. (This turns out not to be a very crucial problem.) Binding energies and shifts $\delta r_{p,n}^2$ and $\delta r_{p,n}^4$ calculated with the SkM* and SIII interactions are shown in Tables 4.1 and 4.2. The binding energies agree in both cases with the experimental values with largest deviation of 4 MeV out of about 1000 MeV of total binding energy.

The comparison between the measured and calculated isotope shifts is illustrated in Figs. 4.2 and 4.3 as a series of successively better approximations. First, the crosses, connected by dashed lines to guide eyes, show the isotope shifts for spherical nuclei. The agreement with experiment is not very good even though the spherical calculation correctly predicts that the slope of the dependence $\delta r_p^2(A)$ is about half of the slope expected from the simple relation $R = r_0 A^{1/3}$. This means that, on average, the neutron-proton interaction we use has the correct magnitude.

Next, the equilibrium deformation for the lighter cesium isotopes is included (open

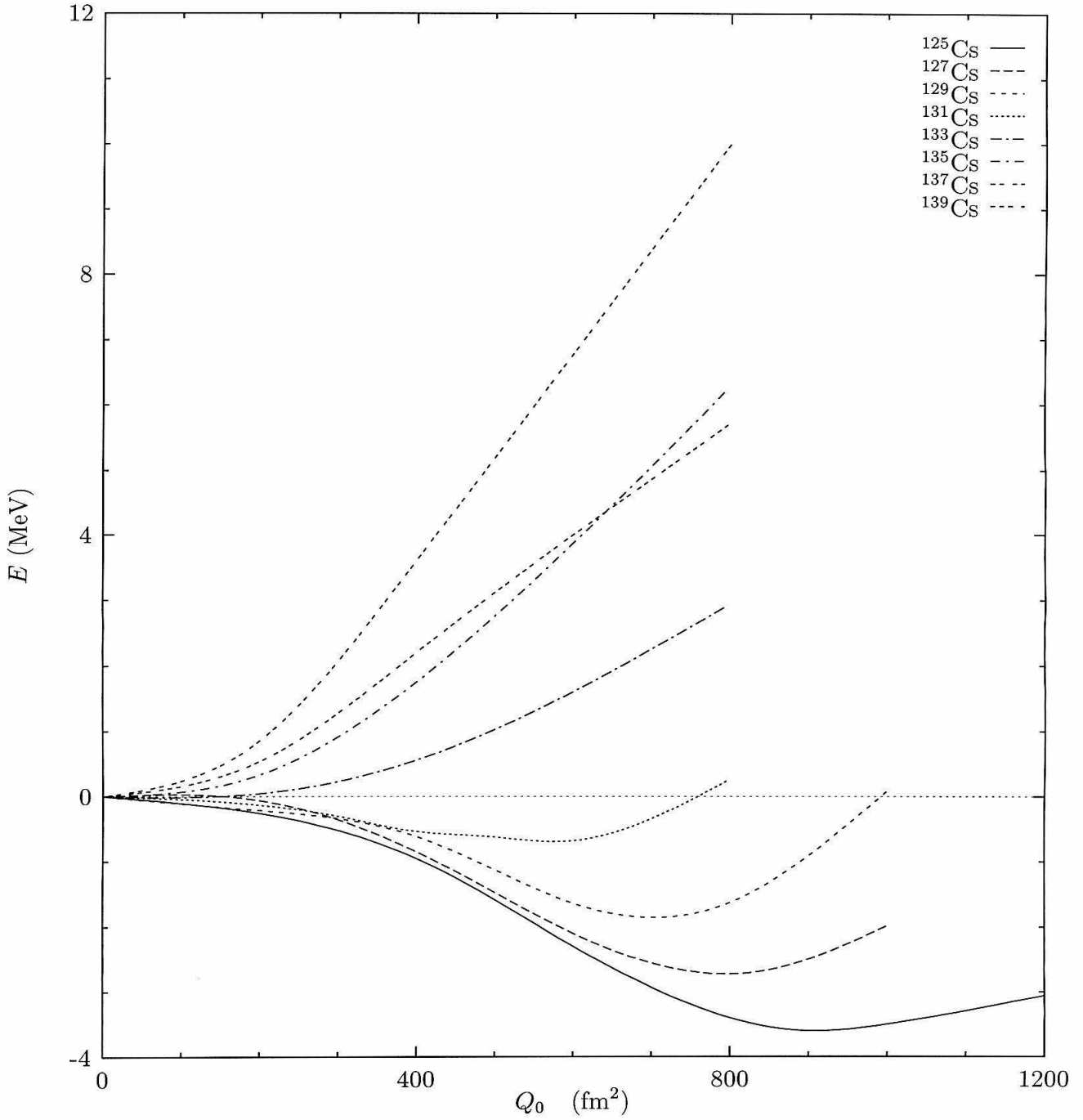


Figure 4.1: The potential energy curves for the isotopes ^{125}Cs – ^{139}Cs calculated by the Hartree-Fock method using the SIII interaction.

Table 4.1: Results of the Hartree-Fock calculations with the SkM* interactions. The experimental binding energies and isotope shifts $\delta\langle r_p^2 \rangle$ are also listed for comparison. (The binding energies are in MeV, all radial moments in fm.) The experimental isotope shifts are from Ref. [55], normalized to the stable isotope ^{133}Cs .

| N | B | B _{HF} | $\delta r_p^2(\text{exp})$ | δr_p^2 | $\delta r_p^2(\text{sph.})$ | δr_p^4 | δr_n^2 | $\delta r_n^2(\text{sph.})$ | δr_n^4 |
|----|---------|-----------------|----------------------------|----------------|-----------------------------|----------------|----------------|-----------------------------|----------------|
| 70 | 1049.98 | 1045.82 | -0.1517 | -0.0899 | -0.4445 | 7.987 | -0.6803 | -1.0787 | -31.126 |
| 72 | 1068.25 | 1064.38 | -0.0985 | -0.0348 | -0.3285 | 8.836 | -0.4603 | -0.7931 | -19.563 |
| 74 | 1085.66 | 1082.15 | -0.0561 | -0.0199 | -0.2161 | 6.247 | -0.2927 | -0.5186 | -11.931 |
| 76 | 1102.37 | 1099.36 | -0.0141 | 0.0090 | -0.1070 | 4.306 | -0.1253 | -0.2544 | -4.538 |
| 78 | 1118.52 | 1117.69 | 0.0000 | 0.0000 | 0.0000 | 0.000 | 0.0000 | 0.0000 | 0.000 |
| 80 | 1134.24 | 1135.71 | 0.0250 | 0.1054 | 0.1054 | 4.872 | 0.2454 | 0.2454 | 14.025 |
| 82 | 1149.27 | 1152.18 | 0.0821 | 0.2531 | 0.2531 | 9.658 | 0.5132 | 0.5132 | 28.754 |
| 84 | 1159.57 | 1164.16 | 0.3604 | 0.3394 | 0.3394 | 17.820 | 0.8866 | 0.8866 | 59.902 |

Table 4.2: Results of the Hartree-Fock calculations with the SIII interactions. See caption to Table I.

| N | B | B _{HF} | $\delta r_p^2(\text{exp})$ | δr_p^2 | $\delta r_p^2(\text{sph.})$ | δr_p^4 | δr_n^2 | $\delta r_n^2(\text{sph.})$ | δr_n^4 |
|----|---------|-----------------|----------------------------|----------------|-----------------------------|----------------|----------------|-----------------------------|----------------|
| 70 | 1049.98 | 1047.12 | -0.1517 | -0.1322 | -0.5097 | 7.670 | -0.5484 | -1.0265 | -24.683 |
| 72 | 1068.25 | 1065.52 | -0.0985 | -0.1015 | -0.3813 | 6.023 | -0.4141 | -0.7592 | -18.954 |
| 74 | 1085.66 | 1083.44 | -0.0561 | -0.0440 | -0.2536 | 6.317 | -0.2526 | -0.4991 | -11.388 |
| 76 | 1102.37 | 1100.62 | -0.0141 | -0.0096 | -0.1265 | 3.117 | -0.1096 | -0.2461 | -5.198 |
| 78 | 1118.52 | 1118.01 | 0.0000 | 0.0000 | 0.0000 | 0.000 | 0.0000 | 0.0000 | 0.000 |
| 80 | 1134.24 | 1134.75 | 0.0250 | 0.1254 | 0.1254 | 6.530 | 0.2392 | 0.2392 | 14.634 |
| 82 | 1149.27 | 1153.20 | 0.0821 | 0.2508 | 0.2508 | 13.124 | 0.4721 | 0.4721 | 29.191 |
| 84 | 1159.57 | 1161.94 | 0.3604 | 0.4120 | 0.4120 | 22.346 | 0.8674 | 0.8674 | 59.984 |

squares), leading to a much better agreement. Further improvement is achieved when the effect of zero-point quadrupole vibrational motion is taken into account. It is well known that the mean square radius of a vibrating nucleus is increased by [56]

$$\langle r^2 \rangle_\beta = \langle r^2 \rangle_0 \left(1 + \frac{5}{4\pi} \langle \beta^2 \rangle \right). \quad (4.10)$$

We include this effect of the shape fluctuations using the quantities $\langle \beta^2 \rangle$ extracted from the measured transition matrix elements $B(E2, 0^+ \rightarrow 2^+)$ and the relation

$$\langle \beta^2 \rangle = B(E2, 0^+ \rightarrow 2^+) [3ZR_0^2/4\pi]^{-2}. \quad (4.11)$$

We take the average $B(E2)$ of the corresponding Xe and Ba isotopes with neutron numbers $N = 78 - 84$ and correct the radii of ^{133}Cs – ^{139}Cs accordingly, as shown in Figs. 4.2 and 4.3. Thus, further improvement in the comparison with the measured isotope shifts results. (For $N = 84$ the $B(E2)$ values are not known. We use instead the empirical relation between the energy of the lowest 2^+ state and the deformation parameter $B(E2)$ [57].) This correction results in changes in r^2 of 0.2124 fm^2 in ^{133}Cs , 0.1325 fm^2 in ^{135}Cs , 0.0724 fm^2 in ^{137}Cs and 0.1263 fm^2 in ^{139}Cs .

In a fully consistent calculation, one should make a similar correction for the deformed cesium isotopes as well. Since the corresponding $B(E2)$ values for the vibrational states are not known, and the corrections are expected to be small and thus do not have to be known precisely, we assume that the $B(E2)$ for the γ and β vibrational states give together 10 Weisskopf units, same for all deformed cesium isotopes. (With such $B(E2)$ the correction happens to be numerically the same as in the semimagic ^{137}Cs .) We believe this shortcoming explains the somewhat poorer agreement in the deformed cesium isotopes.

Even though the quadrupole 2^+ states contribute most to the mean square radius via Eq. (4.10), other vibrational states, e.g., the octupole 3^- and the giant resonances,

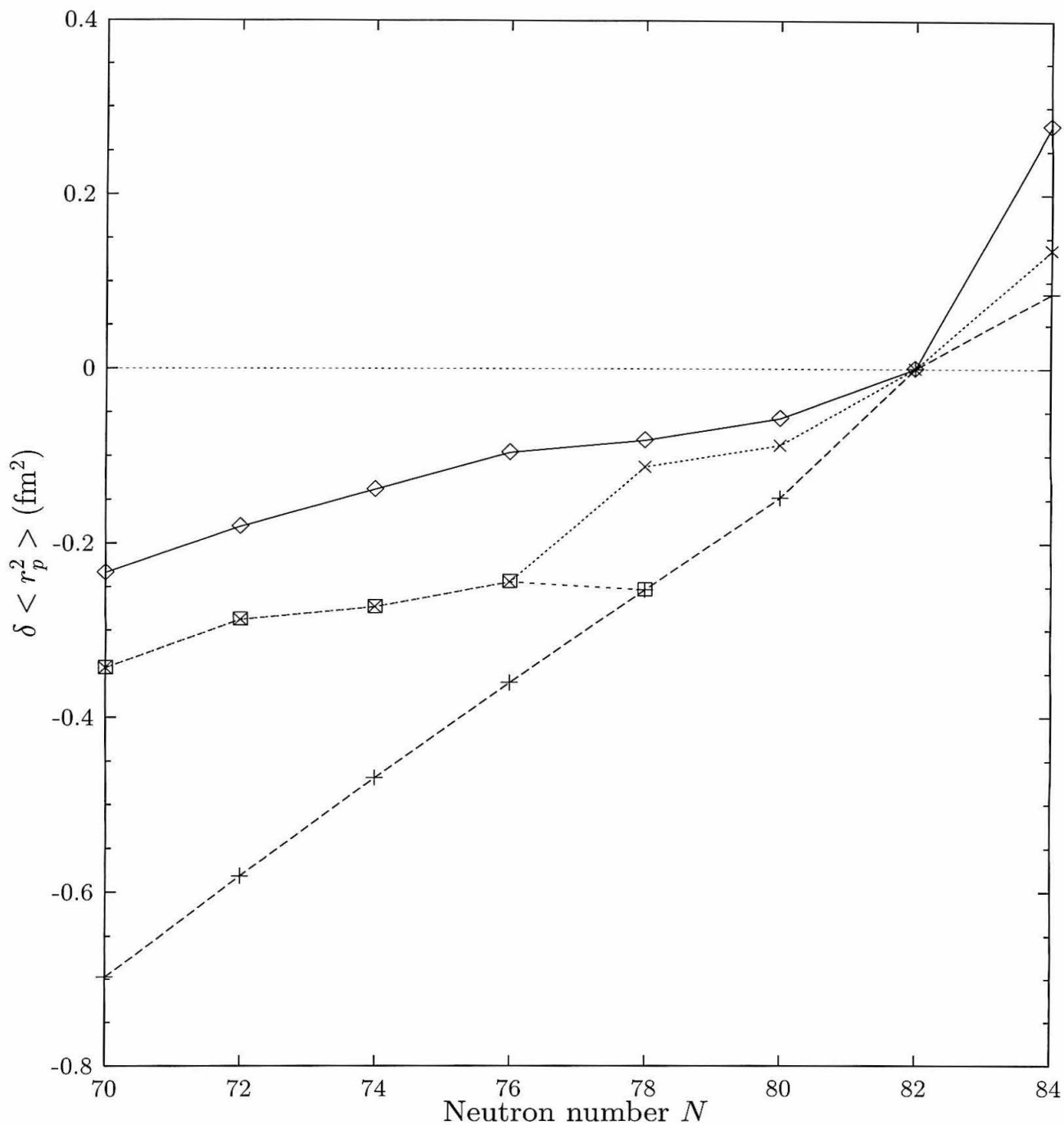


Figure 4.2: Calculated and experimental isotope shifts $\delta \langle r_p^2 \rangle$ in cesium, normalized to the semimagic ^{137}Cs . The SkM* interaction has been used. The correction for zero-point vibrations is described in text. The following notations are used, experimental isotope shift \diamond , spherical HF isotope shifts $+$, HF including equilibrium deformation \square , and corrected for zero-point vibrations \times .

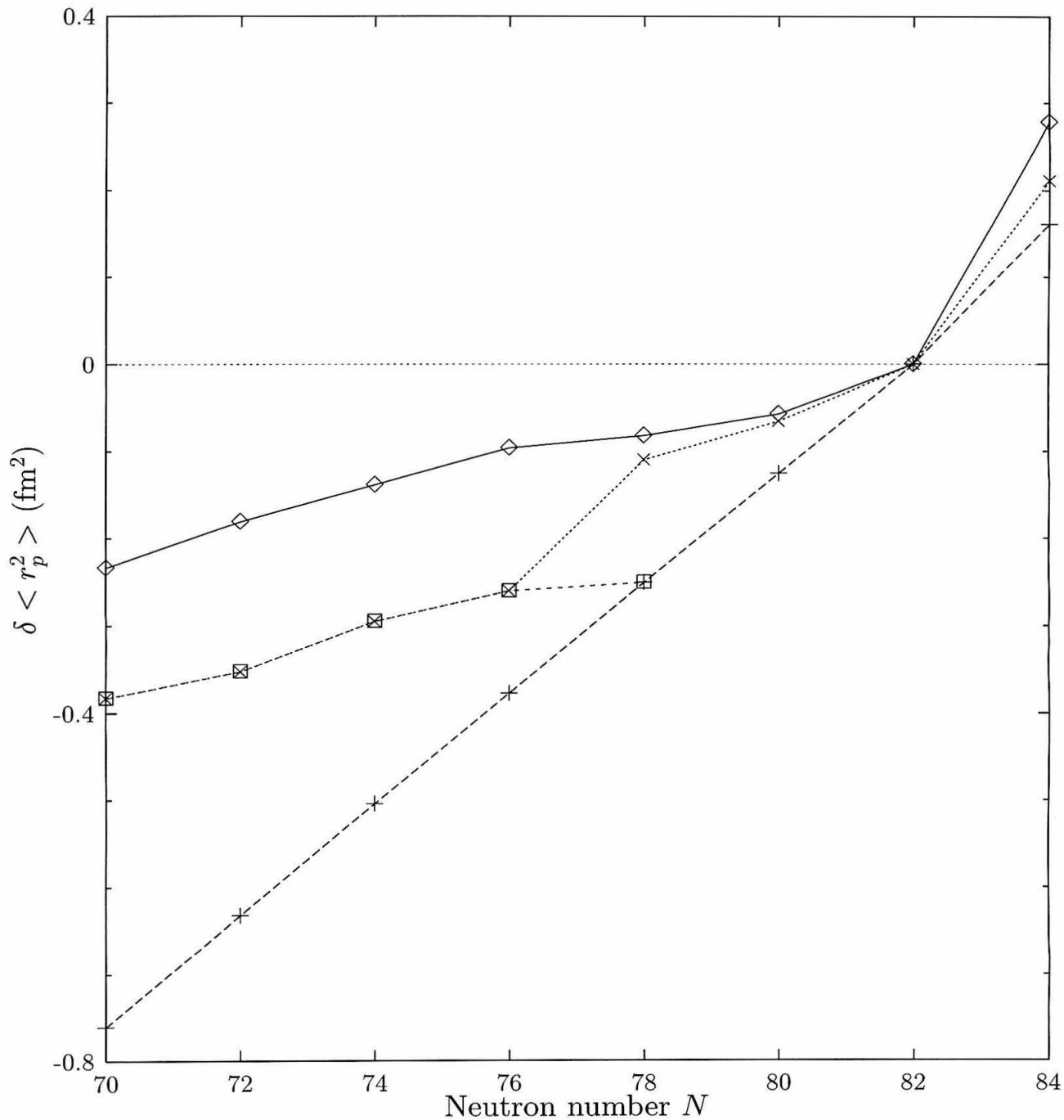


Figure 4.3: Calculated and experimental isotope shifts $\delta \langle r_p^2 \rangle$ in cesium. The SIII interaction has been used. The correction for zero-point vibrations is described in text. Same notations used in fig. 4.2 are used here.

contribute as well; however, all such states not only have smaller collective amplitudes but, even more importantly, vary more smoothly with the atomic mass (or neutron number) than the 2^+ states, and hence their contribution to the shifts δr^2 should be correspondingly smaller.

Altogether, the error in the shift δr_p^2 is at most 0.2 fm^2 , and appears to be independent of the change in the neutron number ΔN . Thus, for the following considerations we assign an uncertainty in the relative value of δr_p^2 of 0.2 fm^2 . Very little is known experimentally about the moments r_p^4 . Quite conservatively, we assume that the uncertainty in δr_p^4 is $\langle r_p^2 \rangle \times \Delta r_p^2 \simeq 5 \text{ fm}^4$.

In a recent similar HF calculation of the charge radii of the Pb isotopes using SkM* and SIII forces, Tajima *et al.*[58] showed that both SIII and SkM* failed to reproduce the experimental charge radii kink across the ^{208}Pb shell closure, even though both forces give excellent agreement with the experimental $\langle r_p^2 \rangle$ on the neutron deficient side. Such failure to reproduce the charge radii kink is also observed in our calculations; however, it is not a serious problem in our case because there is only one isotope above the $N = 82$ shell closure in our calculations. Moreover, the calculations of Ref. [58] confirm our estimate of the error in the shift δr_p^2 , even though the isotope shifts are larger in lead than in cesium.

Before turning our attention to the neutron radii, it is worthwhile to make a brief comment about the comparison with *absolute* values of $\langle r_p^2 \rangle$ and $\langle r_p^4 \rangle$. Experimentally, muonic x-ray energies for the stable ^{133}Cs have been fitted to the Fermi distribution with the halfway radius $c = 5.85 \text{ fm}$, surface thickness $t = 1.82 \text{ fm}$ [59, 60], and $\langle r_p^2 \rangle = 23.04 \text{ fm}^2$. Such a Fermi distribution gives $\langle r_p^4 \rangle = 673 \text{ fm}^4$. Our HF calculation corrected for zero-point vibrational motion with $\langle \beta^2 \rangle = 0.024$, as described above, gives $\langle r_p^2 \rangle_{HF} = 23.27 \text{ fm}^2$ for SIII and 22.69 fm^2 for SkM* interaction, both quite close to the experimental value. The calculated $\langle r_p^4 \rangle$ moments (not corrected for the zero-point motion) are 671(SIII) and 652(SkM*) fm^4 . We see, therefore, that the calculation is quite

successful in the absolute radii (and even surface thicknesses), in particular for the SIII interaction (which also gives the correct ground state spin).

The calculated shifts in the neutron radii δr_n^2 are listed in Tables 4.1 (SkM*) and 4.2 (SIII) and the quantities δr_n^2 corrected for the effect of zero-point vibrational motion are displayed in Fig. 4.4. Several comments about these are in order. First, the slope of the dependence of $\delta r_n^2(A)$ for spherical configurations is correspondingly steeper than the slope following from $R = r_0 A^{1/3}$. That is obviously a correct result; the combination of a smaller slope in the proton radii and a larger slope in the neutron radii when neutrons are added is necessary to maintain on average the $R = r_0 A^{1/3}$ relation. Second, the HF calculations imply that the proton and neutron distributions have essentially identical deformations. This agrees with the general conclusion about the isoscalar character of low-frequency collective modes in nuclei (see, e.g., Ref. [61]). Thus, we accept this result and do not assign any additional uncertainty to the possible difference in the deformation of protons and neutrons. To quantify this statement, recall that a typical deformation for cesium is $\beta = \sqrt{\langle \beta^2 \rangle} \approx 0.2$; from Eq. (4.10) and the requirement $\delta r^2 \leq 0.2 \text{ fm}^2$ we find $\delta\beta/\beta \leq 0.3$. Our assumption means, therefore, that the proton and neutron deformations agree to within 30%, a rather mild restriction. Finally, for the same reason, we use the same $B(E2)$ values, and the $\langle \beta^2 \rangle$ extracted from them, to correct the neutron radii using Eq. (4.10). Assuming all of the above, we assign *identical* uncertainties to the neutron shifts δr_n^2 and the proton shifts δr_p^2 , and similarly to the fourth moments $\delta r_{n,p}^4$.

Very little reliable experimental information on the neutron distribution in nuclei is available. In Ref. [62], data from pionic atoms are analyzed. The corresponding best fit for neutron mean square radii agrees very well with the HF results quoted there. The nearest nucleus to cesium in Ref. [62] is ^{142}Ce . Scaling it with $A^{2/3}$ one arrives at $\langle r_n^2 \rangle = 24.7 \text{ fm}^2$ for ^{133}Cs , somewhat larger than our calculated values 23.7 and 24.0 for SkM* and SIII, respectively. In Ref. [51], the theoretical neutron density of Brack *et al.* [63] with $\langle r_n^2 \rangle = 23.5 \text{ fm}^2$ was used. That value, presumably obtained by interpolation from

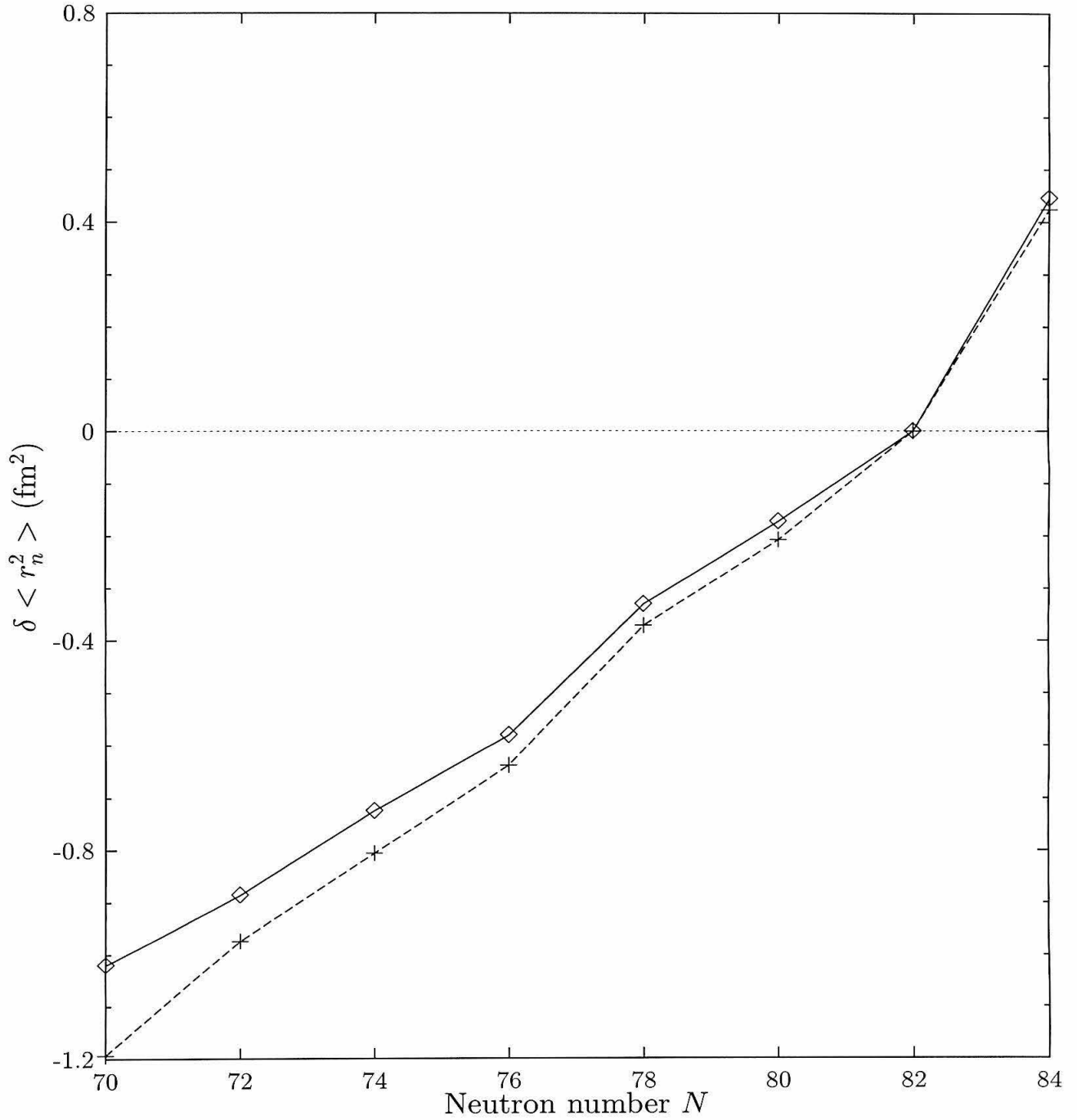


Figure 4.4: Calculated changes in the neutron radii $\delta \langle r_n^2 \rangle$ in cesium. The results, corrected for zero-point vibrational motion, and calculated with the SIII (\diamond) and SkM* (+) interactions, are shown.

the values obtained by the HF method using the SkM* interaction, is, not surprisingly, quite close to our calculated values. This limited comparison suggests that the absolute radii $\langle r_n^2 \rangle$ have uncertainties of about 1 fm^2 . The uncertainty in the shifts δr_n^2 should be substantially smaller, and our estimated error of 0.2 fm^2 does not seem unreasonable.

In Ref. [54] the uncertainty in the integrals $q_{n,p}$ was estimated from the spread of the calculated values with a wide variety of interactions. Some of the interactions employed in [54] give better agreement for known quantities (charge radii, binding energies, etc.) than others. We chose to use only the two most successful interactions. The spread in the calculated shifts $\delta r_{p,n}^2$ for these two interactions is less than our postulated error of 0.2 fm^2 .

In this context it is worthwhile to mention the calculations of Ref. [64]. There, proton and neutron radii for several nuclei were evaluated using Hartree-Fock method with the SIII and SkM* interactions, as in the present work, but also within the relativistic mean-field approach. The HF results with Skyrme forces seem to agree somewhat better with the empirical data, particularly for the heavier nuclei, and our estimated uncertainty of 1 fm^2 for $\langle r_n^2 \rangle$ in a *single* nucleus agrees with the findings of [64]. (This also supports our choice of the method and interaction.) The only pair of isotopes considered in [64] are ^{116}Sn and ^{124}Sn . The calculated δr_n^2 deviate from the empirical ones by less than 0.3 fm^2 ; i.e., the error is somewhat larger than our assumed error. However, when the experimental uncertainty of about 0.5 fm^2 is taken into account, that discrepancy loses significance.

Pollock *et al.* [54] also argue that the isovector surface term $(\rho_p - \rho_n)\nabla^2(\rho_p - \rho_n)$ in the Skyrme Lagrangian is poorly determined and may affect the neutron skin significantly, without affecting most bulk nuclear properties. We tested this claim by modifying simultaneously the coefficients $B_5 \rightarrow B_5(1+x)$ and $B_6 \rightarrow B_6 - 2B_5x$ in Eq. (3.4). We find that when we vary x (i.e., the relative strength of the isovector surface term) from $+0.3$ to -0.3 the proton radius $\langle r_p^2 \rangle$ changes indeed very little (about 0.06 fm^2) and the

neutron radius changes somewhat more (by about 0.1 fm^2 , still far less than our estimated error for an individual nucleus). The effect on the quantity δr_n^2 is substantially less. At the same time, the binding energy changes by about 5 MeV, more than the largest discrepancy between the theory and experiment. Thus, even a quite substantial change in the isovector surface term will affect the neutron radii (and the difference in neutron radii) by less than our assumed error. At the same time such a modification would clearly spoil the agreement with experiment in the binding energies.

We stressed above that there is essentially no model independent experimental information on neutron density distributions. Thus, our calculations, and our estimated uncertainties, cannot be verified directly. Instead, we assume that there are no effects which would change the neutron radii substantially, but would not affect the binding energies, proton radii, or other quantities that are well described by the HF method. We are not aware of any such effects, but one has to be aware of this possibility.

4.4 Estimated uncertainties in PNC effects

The nuclear-structure effects are governed by the coefficients $q_{n,p}$, Eq. (4.5), which in turn involve integrals of the formfactors $f(r)$, Eq. (4.6). The function $f(r)$ is slowly varying over the nuclear volume, and may be accurately approximated by a power series

$$f(r) = 1 + f_2 \times r^2 + f_4 \times r^4, \quad (4.12)$$

and, therefore,

$$q_{n,p} = 1 + f_2 \times \langle r_{n,p}^2 \rangle + f_4 \times \langle r_{n,p}^4 \rangle. \quad (4.13)$$

For a sharp nuclear surface density distribution, the only relevant parameter is the nuclear radius R and $\langle r^{2n} \rangle = 3/(2n+3)R^{2n}$. Using the experimental $\langle r^2 \rangle = 23.04 \text{ fm}^2$

for ^{133}Cs [59], we find from Eq. (4.6)

$$f(r) \simeq 1 - 2.10 \times 10^{-3} r^2 + 1.09 \times 10^{-5} r^4, \quad (4.14)$$

where the distance is measured in fermis. However, as pointed out above, the analytic expansion, Eq. (4.6), is unsuitable at the intended level of accuracy. So, instead, we solve numerically the Dirac equation for the $s_{1/2}$ and $p_{1/2}$ bound electron states in the field of the finite size diffuse surface nucleus, we obtain by fitting the coefficients $f_2(f_4)$ of $-2.31 \times 10^{-3}(1.21 \times 10^{-5})$ when we use the standard surface thickness parameter $t = 2.25$ fm, and $-2.267 \times 10^{-3}(1.157 \times 10^{-5})$ when we use the surface thickness $t = 1.82$ fm adjusted so that the nuclear density parametrized by the two-parameter Fermi distribution resembles as closely as possible the Hartree-Fock charge density in ^{133}Cs . Also, we make sure that the expansion, Eq. (4.12), is accurate over the whole nuclear volume, and that it is sufficient to use only the r^2 and r^4 terms in it.

The expansion coefficients f_2, f_4 depend, primarily, on the mean square charge radius. To take this dependence into account, we use for ^{133}Cs the f_2 and f_4 above, and for the other isotopes, we use the same surface thickness parameter ($t = 1.82$) fm as determined by the Hartree-Fock calculation in ^{133}Cs and adjust the halfway radius in such a way that the experimental $\langle r_p^2 \rangle$ are correctly reproduced.

It is easy now to evaluate the uncertainty in the factors $q_{n,p}$ given the coefficients f_2, f_4 and our estimates of the uncertainties in $\langle r^2 \rangle$ and $\langle r^4 \rangle$. Substituting the corresponding values, we find that the uncertainty is $\delta q_{n,p} = 4.6 \times 10^{-4}$, caused almost entirely by the uncertainty in the mean square radii $\langle r_{n,p}^2 \rangle$. This uncertainty represents about 1% of the deviations of $q_{n,p}$ values from unity.

Before evaluating the nuclear structure corrections $Q_W^{nuc}(N, Z)$ we have to consider

the effect of the intrinsic nucleon structure. Following [54] we use

$$q_{p,n}^{\text{int}} = \int d^3\mathbf{r} \frac{1}{6} \langle r^2 \rangle_{\text{int},(p,n)}^w f(r) \nabla^2 \rho_{p,n} / Q_{p,n}^w , \quad (4.15)$$

where $\langle r^2 \rangle_{\text{int}}^w$ are the nucleon weak radii, and $Q_{p,n}^w$ are the nucleon weak charges. Neglecting the “strangeness radius” of the nucleon, and using the fitted two-parameter Fermi density distribution, we find

$$q_p^{\text{int}} = -0.00290, \quad q_n^{\text{int}} = -0.00102 , \quad (4.16)$$

very close to the sharp nuclear surface values of Pollock *et al.* [54]. The above intrinsic nucleon-structure corrections are small, but not negligible. More importantly, they are independent of the nuclear structure, and cancel out in the differences $\Delta q_{n,p}$.

The quantities $100 \times (q_n - 1)$ and $100 \times (q_p - 1)$ are listed in Table 4.3 for all cesium isotopes and for the two Skyrme interactions we consider. One can see that they vary by about 4% for neutrons and are essentially constant for protons when the neutron number increases from $N = 70$ to 84. The variation with N is essentially identical for the two forces, while the small difference between the $q_{n,p}$ values calculated with the two forces reflects the difference in the *absolute* values of radii for the two interactions.

The weak charges $Q_W(N, Z)$ and the nuclear structure corrections $Q_W^{\text{nuc}}(N, Z)$ in Table 4.3 are radiatively corrected. Thus, instead of the formulas (4.8) and (4.9) we use

$$\begin{aligned} Q_W(N, Z) &= 0.9857 \times [-N + Z(1 - 4.012\bar{x})] \times (1.0 + 0.00782T) , & (4.17) \\ \bar{x} &= 0.2323 + 0.00365S - 0.00261T , \end{aligned}$$

following [43]. Here S is the parameter characterizing the isospin-conserving “new”

Table 4.3: The radiatively corrected weak charges $Q_W(N, Z)$, nuclear structure corrections $Q_W^{\text{nuc}}(N, Z)$, and the quantities $q_n - 1$, $q_p - 1$ (the factors $(q_{p,n} - 1)$ contain the intrinsic nucleon structure correction, and are multiplied by 100 for easier display) calculated with the SkM* and SIII interactions, and with the vibrational corrections described in the text.

| N | $Q_W(N, Z)$ | SkM* | | | SkmIII | | |
|----|-------------|--------------------------|-----------|-----------|--------------------------|-----------|-----------|
| | | $Q_W^{\text{nuc}}(N, Z)$ | $q_n - 1$ | $q_p - 1$ | $Q_W^{\text{nuc}}(N, Z)$ | $q_n - 1$ | $q_p - 1$ |
| 70 | -65.312 | 2.967 | -4.55 | -4.64 | 3.015 | -4.62 | -4.74 |
| 72 | -67.283 | 3.077 | -4.58 | -4.64 | 3.118 | -4.64 | -4.74 |
| 74 | -69.254 | 3.184 | -4.60 | -4.64 | 3.225 | -4.66 | -4.75 |
| 76 | -71.226 | 3.291 | -4.62 | -4.64 | 3.330 | -4.68 | -4.75 |
| 78 | -73.197 | 3.422 | -4.68 | -4.68 | 3.458 | -4.73 | -4.79 |
| 80 | -75.169 | 3.528 | -4.69 | -4.67 | 3.564 | -4.74 | -4.79 |
| 82 | -77.140 | 3.638 | -4.71 | -4.68 | 3.669 | -4.76 | -4.79 |
| 84 | -79.112 | 3.745 | -4.73 | -4.66 | 3.780 | -4.78 | -4.78 |

quantum loop corrections, and T characterizes the isospin-breaking corrections [65]. Also,

$$Q_W^{\text{nuc}}(N, Z) = 0.9857 \times [-N(q_n - 1) + Z(1 - 4.012\bar{x})(q_p - 1)] . \quad (4.18)$$

These quantities, evaluated for $S = T = 0$, are shown in Table III. The assumed uncertainty in the shifts of the mean square radii, and consequently in the changes in factors $q_{n,p}$ results in the relative uncertainty $\delta Q_W/Q_W$ of 5×10^{-4} . That uncertainty, therefore, represents within the nuclear model we use, the “ultimate” nuclear structure limitation on the tests of the Standard Model in the atomic PNC experiments involving several isotopes.

In the atomic PNC experiments involving a *single* isotope, the uncertainty in the neutron mean square radius is larger, and 1 fm^2 appears to be a reasonable choice. Thus, from nuclear structure alone, the weak charge in a single isotope has relative uncertainty of about 2.5×10^{-3} , perhaps comparable to the best envisioned measurements, but consid-

erably smaller than the present uncertainty associated with the *atomic* structure. (The five times larger uncertainty 2.5×10^{-3} for a single isotope, as opposed to the uncertainty 5×10^{-4} in the previous paragraph for a series of isotopes, is a consequence of the five time larger *absolute* uncertainty in $\langle r_n^2 \rangle$ as opposed to the uncertainty in the shift δr_n^2 .)

Suppose now that in an experiment involving several cesium isotopes one is able to determine the ratio

$$R(N', N) = \frac{Q_W(N', Z) + Q_W^{\text{nuc}}(N', Z)}{Q_W(N, Z) + Q_W^{\text{nuc}}(N, Z)} \quad (4.19)$$

with some relative uncertainty $\delta R/R$. To a (reasonable) first approximation

$$R(N', N) \approx \frac{Q_W(N', Z)}{Q_W(N, Z)} \times [1 + q_n(N') - q_n(N)] . \quad (4.20)$$

Thus, we see that nuclear structure contributes to the uncertainty of R at the level of roughly 7×10^{-4} , where we added the individual errors in quadrature. This uncertainty is much smaller than the anticipated experimental error.

In such a measurement, therefore, the uncertainty in \bar{x} will be

$$\frac{\delta \bar{x}}{\bar{x}} \approx \frac{\delta R}{R} \times \frac{NN'}{Z\Delta N} \approx 8 \frac{\delta R}{R} , \quad (4.21)$$

(see also [43, 54]) where the last factor is evaluated for $N', N = 70, 84$. The above equation illustrates the obvious advantage of using isotopes with large ΔN . Also, by performing the measurement with several isotope pairs, one can further decrease the uncertainty $\delta \bar{x}$.

When considering restrictions (or determination) of the parameters S and T [65] one has to distinguish the PNC experiments involving a single isotope or several isotopes. In a single isotope the contributions involving T largely cancel, and one is left with sensitivity to S only. On the other hand, for several isotopes, and taking ratios, *both* S and T contribute. The uncertainty in the parameters S and T is determined to good

approximation from the relation $\delta\bar{x} = 0.00365\delta S - 0.00261\delta T$, and thus

$$\delta S \approx \frac{\delta R}{R} \times \frac{NN'}{0.014Z\Delta N}, \quad \delta T \approx \frac{\delta R}{R} \times \frac{NN'}{0.010Z\Delta N}. \quad (4.22)$$

4.5 Conclusion

In conclusion, we have evaluated the nuclear structure corrections to the weak charges for a series of cesium isotopes, and estimated their uncertainties. Within the model we used, i.e., the Hartree-Fock method with Skyrme interaction, with deformation and zero point motion corrections added as described above, we concluded that the imperfect knowledge of the neutron distribution in cesium isotopes does not represent in the foreseeable future a limitation on the accuracy with which the Standard Model could be tested in the atomic PNC experiments.

Bibliography

- [1] T.H.R. Skyrme, *Phil. Mag.* **1**, 1043 (1956); *Nucl. Phys.* **9**, 615 (1959)
- [2] D. Vautherin and D.M Brink, *Phys. Rev.* **C5** , 626 (1972) .
- [3] M. Beiner, H. Flocard, Nguyen Van Giai, and P. Quentin, *Nucl. Phys.* **A238** , 29 (1975)
- [4] X. Campi and M. Epherre, *Phys. Rev.* **C22** (1980) 2605
- [5] J.M.G. Gomez, C. Prieto and J. Navarro *Nucl. Phys.* **A549** (1992) 125
- [6] J. Bartel, P. Quentin, M. Brack, C. Guet, and H. B. Hakansson, *Nucl. Phys.* **A386** , 79 (1982).
- [7] H. Krivine, J. Treiner and O. Bohigas, *Nucl. Phys*, **A336** (1980) 155
- [8] P. Bonche, H. Flocard, P.-H. Heenen, S.J. Krieger and M.S. Weiss, *Nucl. Phys.* **A443** , 39 (1985) .
- [9] H. Flocard, P. Quentin, A.K. Kerman and D. Vautherin *Nucl. Phys.* **A203** , 433 (1973)
- [10] M. Abramowitz and I.A. Stegun, *Handbook of mathematical functions* (Dover, 1965) p. 887

- [11] P.H. Heenen, P. Bonche and H. Flocard, Proc. Conf. on TDHF, Gif/Yvette
P. Bonche, B. Giraud and P. Quentin (Edition de Physique, Paris, 1979) 175
- [12] K.T.R. Davies, *et al.*, Nucl. Phys. **A342** (1980) 111
- [13] S.G. Nilson. Mat. Fys. Medd. Dan. Vid. Selsk. **29** (1955) No. 16, 68, 70, 71, 72, 76
- [14] P.J. Twin *et al.*, Phys. Rev. Lett. **57** (1986) 811
- [15] E.F. Moore *et al.*, Phys. Rev. Lett. **63** (1989) 360
- [16] P.J. Nolan and P.J. Twin, Ann. Rev. Nucl. Part. Sci. **38** (1988) 533
- [17] T. Byrsky, *et al.*, Phys. Rev. Lett. **60** (1990) 503
- [18] B. Hass, *et al.*, Phys. Rev. **C42** (1990) R1817
- [19] F.S. Stephens, Nucl. Phys. **A520** (1990) 91c
- [20] W. Satula, S. Ówiok, W. Nazarewicz, R. Wyss and A. Johnson Nucl. Phys. **A529**
(1991) 289
- [21] D. Ye *et al.*, Phys. Rev. **C41** (1990) R13
- [22] J.A. Becker, N. Roy, E.A. Henry, M.A. Deleplanque, C.W. Beausang, R.M. Dia-
mond, J.E. Draper, F.S. Stephens, J.A. Cizewski and M.J. Brinkman, Phys. Rev.
C41 (1990) R9
- [23] M.J. Brinkman *et al.*, Z. Phys. **A336** (1990) 115
- [24] K. Theine *et al.*, Z. Phys **A336** (1990) 113
- [25] H. Hübel *et al.*, Nucl. Phys. **A520** (1990) 125c
- [26] E.A. Henry *et al.*, Z. Phys **A335** (1990) 361

- [27] M. Riley et al., Nucl. Phys. **A512** (1990) 178
- [28] C. Baktash et al., Contribution to the Int. Conf on Nuclear Structure at High Angular momenta, p 60, Ottawa 1992.
- [29] I. Ahmad, M.P. Carpenter, P.R. Chasman, R.V.F. Janssens and T.L. Khoo, Phys. Rev. **C44** (1991) 1204
- [30] R.F. Casten, N.V. Zamfir, P. von Brentano and W.-T. Chou, Phys. Rev. **C45** (1992) 1413
- [31] I. Ragnarsson, Nucl. Phys. **A520** (1990) 67c
- [32] J. Dudek Z. Szymanski and T. Werner, to be published.
- [33] W. Nazarewicz et al., Phys. Rev. Lett. **64** (1990) 1654
- [34] M. Girod, J.P. Delaroche, J. Libert and I. Deloncle, Phys. Rev. **C45** (1992) 1420
- [35] Y. Engel, D.M. Brink, K. Goeke, S.J. Krieger, and D. Vautherin, Nucl. Phys. **A249** (1975) 215
- [36] P. Bonche, H. Flocard and P.-H. Heenen, Nucl. Phys. **A467** (1987) 115
- [37] M. Meyer, N. Redon, Ph. Quentin and J. Libert Phys. Rev. C **45** (1992) 233
- [38] R.R. Chasman, Phys. Lett. **B219** (1989) 227
- [39] E. Moore et al., Phys. Rev. Lett. **64** (1990) 3127
- [40] P.J. Twin et al., Nucl. Phys. **A522** (1991) 13c
- [41] R. Janssens and T. Khoo, Ann. Rev. Nucl. Part. Sci. **41** (1991) 321
- [42] P. Langacker, M.-X. Luo, and A. K. Mann, Rev. Mod. Phys. **64**, 87 (1992).

- [43] W. Marciano and J. Rosner, *Phys. Rev. Lett.* **65**, 2963 (1990).
- [44] V. V. Flambaum, I. B. Khriplovich, and O. P. Sushkov, *Phys. Lett* **146B**, 367 (1984).
- [45] W. C. Haxton, E. M. Henley, and M. J. Musolf, *Phys. Rev. Lett.* **63**, 949 (1989).
- [46] M. C. Noecker, B. P. Masterson, and C. Wieman, *Phys. Rev. Lett.* **61**, 310 (1988).
- [47] M. A. Bouchiat *et al.*, *Phys. Lett.* **117B**, 358 (1982); **134B**, 463 (1984); *J. Phys. (Paris)* **47**, 1709 (1986).
- [48] E. D. Commins, *Phys. Scr.* **36**, 468 (1987).
- [49] V. L. Telegdi, in *Fundamental Symmetries in Nuclei and Particles*, eds. H. Henrikson and P. Vogel, World Scientific, Singapore, 1990.
- [50] C. Wieman, C. Monroe, and E. A. Cornell, in *Laser Spectroscopy X*, eds. M. Ducloy, E. Jacobino, and G. Camy, World Scientific, Singapore, 1991.
- [51] S. A. Blundell, W. R. Johnson, and J. Sapirstein, *Phys. Rev. Lett.* **65**, 1411 (1990).
- [52] V. Dzuba, V. Flambaum, and O. Sushkov, *Phys. Lett.* **141A**, 147 (1989).
- [53] E. N. Fortson, Y. Pang, and L. Wilets, *Phys. Rev. Lett.* **65**, 2857 (1990).
- [54] S. J. Pollock, E. N. Fortson, and L. Wilets, *Phys. Rev.* **C46**, 2587 (1992).
- [55] C. Thibault *et al.*, *Nucl. Phys* **A367**, 1 (1981).
- [56] A. Bohr and B. R. Mottelson, in *Nuclear Structure, Vol. I*, p. 164. Benjamin, Reading, 1975.
- [57] S. Raman, C. W. Nestor, and K. H. Bhatt, *Phys. Rev. C* **37**, 805 (1988).
- [58] N. Tajima, P. Bonche, H. Flocard, P.-H. Heenen and M.S. Weiss *Nucl. Phys.* **A551**, 434 (1993)

- [59] R. Engfer *et al.*, ADNDT **14**, 509 (1974).
- [60] W. Y. Lee *et al.*, Phys. Rev. Lett. **23**, 648 (1969).
- [61] A. Bohr and B. R. Mottelson, *Nuclear Structure*, (Benjamin, Reading, MA, 1975), Vol. II, p.383
- [62] C. Garcia-Recio, J. Nieves, and E. Oset, Nucl. Phys. **A547**, 473 (1992).
- [63] M. Brack, C. Guet, and H.-B. Hakansson, Phys. Rep. **123**, 275 (1975).
- [64] M. M. Sharma and P. Ring, Phys. Rev. C **45**, 2514 (1992).
- [65] M. E. Peskin and T. Takeuchi, Phys. Rev. Lett. **65**, 964 (1990).